

## A case study of observations of volcanic ash from the Eyjafjallajökull eruption: 2. Airborne and satellite radiative measurements

Stuart M. Newman,<sup>1</sup> Lieven Clarisse,<sup>2</sup> Daniel Hurtmans,<sup>2</sup> Franco Marengo,<sup>1</sup> Ben Johnson,<sup>1</sup> Kate Turnbull,<sup>1</sup> Stephan Havemann,<sup>1</sup> Anthony J. Baran,<sup>1</sup> Debbie O'Sullivan,<sup>1</sup> and Jim Haywood<sup>1,3</sup>

Received 25 August 2011; revised 14 December 2011; accepted 16 December 2011; published 21 February 2012.

[1] An extensive set of airborne and satellite observations of volcanic ash from the Eyjafjallajökull Icelandic eruption are analyzed for a case study on 17 May 2010. Data collected from particle scattering probes and backscatter lidar on the Facility for Airborne Atmospheric Measurements (FAAM) BAe 146 aircraft allow estimates of ash concentration to be derived. Using radiative transfer simulations we show that airborne and satellite infrared radiances can be accurately modeled based on the in situ measured size distribution and a mineral dust refractive index. Furthermore, airborne irradiance measurements in the 0.3–1.7  $\mu\text{m}$  range are well modeled with these properties. Retrievals of ash mass column loading using Infrared Atmospheric Sounding Interferometer (IASI) observations are shown to be in accord with lidar-derived mass estimates, giving for the first time an independent verification of a hyperspectral ash variational retrieval method. The agreement of the observed and modeled solar and terrestrial irradiances suggests a reasonable degree of radiative closure implying that the physical and optical properties of volcanic ash can be relatively well constrained using data from state-of-the-science airborne platforms such as the FAAM BAe 146 aircraft. Comparisons with IASI measurements during recent Grímsvötn and Puyehue volcanic eruptions demonstrate the importance of accurately specifying the refractive index when modeling the observed spectra.

**Citation:** Newman, S. M., L. Clarisse, D. Hurtmans, F. Marengo, B. Johnson, K. Turnbull, S. Havemann, A. J. Baran, D. O'Sullivan, and J. Haywood (2012), A case study of observations of volcanic ash from the Eyjafjallajökull eruption: 2. Airborne and satellite radiative measurements, *J. Geophys. Res.*, 117, D00U13, doi:10.1029/2011JD016780.

### 1. Introduction

[2] The eruption of the Eyjafjallajökull Icelandic volcano during the period 14 April to 21 May 2010 caused unprecedented disruption to European airspace. This was due to the advection of volcanic ash particles over much of Europe, which are known to damage jet engines if encountered at sufficient concentrations [Guffanti *et al.*, 2010; Witham *et al.*, 2007]. During this episode the monitoring of ash spatial distributions from satellite radiance measurements played an important role in the tracking of aerosol plumes and in the validation of ash dispersion forecasts. As well as highlighting the importance of satellite data in ash detection

the incident motivated further research into the quantitative retrieval of ash concentrations from space.

[3] Operational retrievals of aerosol optical depths and column burdens have been extensively developed using multiple wavelengths in the visible region of the spectrum on polar orbiting satellite platforms (e.g., the Advanced Very High Resolution Radiometer (AVHRR) [Mishchenko *et al.*, 1999]; Clouds and the Earth's Radiant Energy System (CERES) [Loeb and Kato, 2002]; the Moderate Resolution Imaging Spectrometer (MODIS) [Remer and Kaufman, 2006]; the Multiangle Imaging Spectro-Radiometer (MISR) [Kahn *et al.*, 2001]). Geostationary satellite retrieval algorithms have also been developed at solar wavelengths [e.g., Brindley and Ignatov, 2006] and offer far superior temporal sampling. While the algorithms differ in detail, these retrievals rely on the wavelength-dependent reflection by aerosol of incident sunlight back to space and are only possible during the hours of sunlight in the absence of cloud. Additionally, many of the visible retrieval algorithms are only performed over well-characterized dark surfaces such as oceans although the use of multiple views [Kahn *et al.*, 2001]

<sup>1</sup>Observation Based Research, Met Office, Exeter, UK.

<sup>2</sup>Spectroscopie de l'Atmosphère, Service de Chimie Quantique et Photoscopique, Université Libre de Bruxelles, Brussels, Belgium.

<sup>3</sup>College of Engineering, Mathematics, and Physical Science, University of Exeter, Exeter, UK.

or UV wavelengths [Hsu *et al.*, 2006] can eliminate this problem.

[4] If aerosols are of large enough sizes, in addition to their impact on solar wavelengths of electromagnetic radiation they may significantly perturb the terrestrial radiation budget by absorbing and emitting terrestrial radiation. This has led to the development of aerosol retrievals for mineral dust and volcanic ash that use thermal infrared channels on polar orbiting [e.g., Prata and Grant, 2001; Watkin, 2003] and geostationary platforms [e.g., Prata and Kerkmann, 2007]. The detection algorithms for multichannel imagers exploit brightness temperature differences between channels at 8–10  $\mu\text{m}$  (sensitive to ash and dust) and 11–12  $\mu\text{m}$  (sensitive to water and ice clouds) and typically use data from two or three wavelengths. When mounted on geostationary platforms, infrared sensors are capable of providing high temporal (e.g., every 15 min for the EUMETSAT Spinning Enhanced Visible and Infrared Imager (SEVIRI) RGB product) monitoring of volcanic ash plumes [see Francis *et al.*, 2012].

[5] A new generation of spaceborne hyperspectral sounders, such as the Atmospheric Infrared Sounder (AIRS) on the Aqua platform and the Infrared Atmospheric Sounding Interferometer (IASI) on MetOp, offer greater information content through much higher spectral resolution. The very high spectral resolution from hyperspectral measurements has already proven extremely useful in monitoring and tracking the evolution of  $\text{SO}_2$  from large volcanic eruptions which can be used to validate numerical model simulations [e.g., Haywood *et al.*, 2010]. The unique signature of volcanic ash in hyperspectral data allows parameters such as aerosol effective radii, concentrations and mass to be remotely sensed with greater confidence than if only a few wavelengths are utilized [Clarisse *et al.*, 2010a; Prata *et al.*, 2010].

[6] The initial explosive eruption of Eyjafjallajökull commenced on 14 April 2010 closing significant amounts of UK and European airspace [Dacre *et al.*, 2011; Schumann *et al.*, 2011; Ansmann *et al.*, 2010]. Unfortunately, the FAAM BAe-146 was out of service when the eruption occurred, but was made operational as soon as possible and commenced active flying on 20 April, making a total of twelve flights dedicated to remote sensing and in situ measurements of volcanic ash (B. T. Johnson *et al.*, In situ observations of volcanic ash clouds from the FAAM aircraft during the eruption of Eyjafjallajökull in 2010, submitted to *Journal of Geophysical Research*, 2011).

[7] In accompanying papers in this special section [Turnbull *et al.*, 2012; Marengo *et al.*, 2011] we describe the in situ and downward-looking lidar data gathered during the UK Facility for Airborne Atmospheric Measurements (FAAM) BAe-146 flight on 17 May 2010, and the corresponding data analysis required to obtain quantitative estimates of ash size distribution, optical extinction and mass loading. Part 1 of this case study [Turnbull *et al.*, 2012] describes the in situ airborne observations on 17 May 2010 obtained from the FAAM BAe-146 and Deutsches Zentrum für Luft- und Raumfahrt (DLR) Falcon aircraft. Turnbull *et al.* [2012, Figure 3] illustrate how geostationary SEVIRI imagery was able to track the volcanic ash plume, with light north to northwesterly winds carrying the ash over the North Sea in otherwise clear sky conditions. In this (Part 2) paper we concentrate on radiation measurements obtained on

17 May 2010 comprising aircraft and satellite radiances and irradiances in the presence of ash, spanning the infrared to visible spectral range. We seek to demonstrate radiative closure between (1) the radiation observations; (2) collocated profiles of aerosol extinction derived from lidar backscatter measurements; (3) aerosol optical properties based on a representative particle size distribution and choice of ash complex refractive index; and (4) radiative transfer simulations. Further, we verify the performance of hyperspectral retrievals of ash mass loadings using IASI observations, providing independent verification of such methods for the first time.

[8] In section 2 of this paper we summarize the aircraft observations relevant to this work, including in situ ash properties and concentrations derived from aircraft probes and lidar backscatter measurements. We describe in section 3 observations from the Met Office airborne radiometers operating at solar and terrestrial wavelengths and show results from radiative transfer modeling. Observations from the IASI infrared sounder on the MetOp satellite and the results of ash mass loading retrievals are detailed in section 4, and we conclude in section 5.

## 2. Measurements and Modeling of Ash Properties

### 2.1. In Situ Ash Measurements

[9] Observations of airborne ash from the eruption of Eyjafjallajökull were made from the UK's FAAM aircraft. A comprehensive overview of the in situ measurements during the flights in April–May 2010 is made by Johnson *et al.* (submitted manuscript, 2011) while Turnbull *et al.* [2012] present analysis of aircraft data from this case study on 17 May 2011. We restrict ourselves here to a brief summary of the aircraft data and derived ash properties.

[10] Aerosol concentrations were measured by wing-mounted optical particle counters: the Particle Measuring System (PMS) Passive Cavity Aerosol Spectrometer Probe 100X (PCASP), with size bins covering the range 0.1–0.6  $\mu\text{m}$  nominal diameter i.e., fine mode aerosol, and the University of Manchester Cloud and Aerosol Spectrometer (CAS) probe covering the size range 0.6–35  $\mu\text{m}$ , i.e., coarse mode. CAS is one of the instruments that comprises the Cloud Aerosol and Precipitation Spectrometer (CAPS). The Small Ice Detector (SID-2H) was also fitted and used to determine the asphericity of particles with diameters greater than 2  $\mu\text{m}$ . The coarse mode aerosols are assumed to be ash, with ash mass concentration derived from integrating over the CAS size distribution; this requires the solid density of ash to be known, in this case an assumed value of 2300  $\text{kg/m}^3$ , and is also sensitive to assumptions regarding particle shape and complex refractive index.

[11] The refractive index used in the present CAS data analysis is based on the mineral dust data set of Balkanski *et al.* [2007] with a 1.5% level of hematite. The use of these high silicate refractive indices is justified by examining the in-flight statistics of airborne volcanic ash collected by filters on the German Falcon aircraft [Schumann *et al.*, 2011] which was flying in close proximity to the BAe 146 aircraft [Turnbull *et al.*, 2012] and sampled the same volcanic ash plume. Schumann *et al.* [2011] report post-flight analysis of 489 individual particles using a scanning electron microscope with an attached energy dispersive X-ray (EDX)

detector. Their analysis reveals that, perhaps rather surprisingly, silicates compose more than 83% of particles between 0.5 and 1.0  $\mu\text{m}$  size, 92% of particles between 1.0 and 2.0  $\mu\text{m}$  and 100% of particles larger than 2.0  $\mu\text{m}$  (only 7 particles sampled for this largest size bin). Note that while *Schumann et al.* [2011] report that the particles are predominantly silicates on 17 May 2010, analysis of the volcanic plume on 2 May 2010 suggest significantly less silicate material present. While our results use the refractive indices from *Balkanski et al.* [2007], we also present a sensitivity analysis of the impacts on retrievals of volcanic ash using other assumed refractive indices and show that our choice gives optimal results across the terrestrial spectrum.

[12] Different assumptions of particle shape, namely spheres and an irregularly shaped model comprising a mixture of hexagonal prisms and polyhedral particles, hereinafter referred to as the “irregular model” (for details of the irregular model, see *Osborne et al.* [2011]), have been tested separately. Ash mass concentrations of up to approximately 500  $\mu\text{g}/\text{m}^3$  (irregular model; 700  $\mu\text{g}/\text{m}^3$  when spheres are assumed with the same effective diameter and extinction but increased number) were encountered during a series of profiles around 54°N, 0–2°E on 17 May 2010. The mass concentrations have an estimated uncertainty of a factor of 2 (Johnson et al., submitted manuscript, 2011) due to uncertainties in particle properties and instrument sizing accuracy.

[13] Additionally, aerosol scattering coefficients were determined at three wavelengths (450 nm, 550 nm, 700 nm) using a TSI 3563 nephelometer on the FAAM BAe-146 via an inlet sampling the external air. Using optical properties calculated from the CAS/PCASP size distributions the aerosol mass was derived from the nephelometer measurements. Combining several intercepts of the ash layer the nephelometer-derived column ash loading was in the range 0.29–0.72  $\text{g}/\text{m}^2$ , compared with 0.22–0.71  $\text{g}/\text{m}^2$  for the CAS data [*Turnbull et al.*, 2012] when obtained with the default irregular model.

## 2.2. Lidar Observations

[14] The Leosphere ALS450 elastic backscatter lidar was deployed on the FAAM BAe 146–301 research aircraft during the Eyjafjallajökull eruption, in a nadir-viewing geometry. *Marenco et al.* [2011] describe the methodology for converting lidar beam returns at 355 nm wavelength into profiles of aerosol extinction, which excludes molecular Rayleigh scattering and cloud returns. It is estimated that the uncertainty in the derived extinction is  $\pm 30\%$ .

[15] Although it is not directly measured by the lidar, it is possible to infer the ash mass concentration by combining lidar extinction with in situ measurements. Key to this derivation are the specific extinction coefficient,  $k_{\text{ext}}$  (units  $\text{m}^2/\text{g}$ ) at the lidar wavelength, and the fraction of aerosol extinction associated with the coarse mode (ash),  $f_c$ , which were determined from PCASP and CAS measurements for each FAAM flight (Johnson et al., submitted manuscript, 2011). Values of  $k_{\text{ext}}$  and  $f_c$  are dependent on assumptions of particle shape, complex refractive index and density. *Marenco et al.* [2011, Table 2] show how these parameters vary from flight to flight, with Mie-Lorenz calculations (spheres) and with the more sophisticated irregular particle model. The assumption of spheres leads to slightly higher lidar-derived mass estimates than with the irregular model (by

approximately 30%). An overall uncertainty of a factor of two is estimated for the lidar mass concentrations derived in this manner.

[16] On 17 May 2010, a peak ash concentration of 800  $\mu\text{g}/\text{m}^3$  (assuming the irregular model), 1100  $\mu\text{g}/\text{m}^3$  (spherical model), was determined from lidar returns, i.e., locally higher than CAS peak values where the FAAM BAe 146 intercepted the ash. (We note that this discrepancy can be explained by the highly spatially variable concentrations of aerosol observed.) The ash plume was observed [*Marenco et al.*, 2011] mainly between 3.5 and 5.6 km altitude and had a typical depth of 1.3 km (up to 2.0 km at times). Its measured east-west horizontal cross section was found to be over 500 km, with a large concentration feature ( $>500 \mu\text{g}/\text{m}^3$ ) only 85 km long. The lidar-derived ash column loading was typically 0.3  $\text{g}/\text{m}^2$ , peaking at 0.75  $\text{g}/\text{m}^2$ , assuming irregular particles (0.4  $\text{g}/\text{m}^2$  peaking at 1.0  $\text{g}/\text{m}^2$  assuming spheres) compared with CAS values of up to 0.7  $\text{g}/\text{m}^2$  (irregulars), 1.0  $\text{g}/\text{m}^2$  (spheres). A map of observed ash column loads derived from the lidar for 17 May is displayed in Figure 4e of *Marenco et al.* [2011].

## 2.3. Ash Optical Properties

[17] A key aim of this paper is to test whether it is possible to obtain radiative closure between: radiation measurements across the visible to infrared spectrum; observations of ash profile concentrations; and simulated radiances and irradiances based on derived optical properties. Here we adopt the spherical assumption for particle shape for calculating infrared optical properties. The aerosol optical properties were calculated via Mie-Lorenz theory using the mineral dust refractive index of *Balkanski et al.* [2007] (Figure 1). The particle size distribution (PSD) was represented by a lognormal distribution as described by *Turnbull et al.* [2012]. The extinction coefficient, single scattering albedo and asymmetry parameter decrease between solar ( $<3 \mu\text{m}$ ) and thermal IR wavelengths ( $>6 \mu\text{m}$ ) and then vary within the IR region as a strong function of refractive index. Note, the infrared wave number region of interest in this study (the atmospheric window situated approximately between 800–1250  $\text{cm}^{-1}$ ) corresponds to wavelengths of 12.5–8.0  $\mu\text{m}$ . The mineral dust hematite concentration has a significant effect on the single scattering albedo in the shortwave spectrum but has insignificant consequence on the longwave properties or the ratio between shortwave and longwave aerosol extinction. Therefore, for consistency with Johnson et al. (submitted manuscript, 2011) and *Turnbull et al.* [2012] we adopt the medium (1.5%) hematite content, as used to calculate the optical properties displayed in Figure 1, for all atmospheric radiative transfer modeling in this study associated with the interpretation of broadband and spectrally resolved radiation measurements. Figure 1 demonstrates how the Mie-Lorenz calculations relate PCASP/CAS measurements of the PSD and lidar-derived vertical extinction profiles at visible and UV wavelengths with measurements in the mid-infrared spectral region.

[18] We aim to test the sensitivity of radiative transfer simulations to assumptions of particle shape and PSD. Applying the spherical and irregular models to the interpretation of CAS data results in different parameterized forms of the PSD. Additionally, we make use of independent optical particle counter measurements from the DLR Falcon

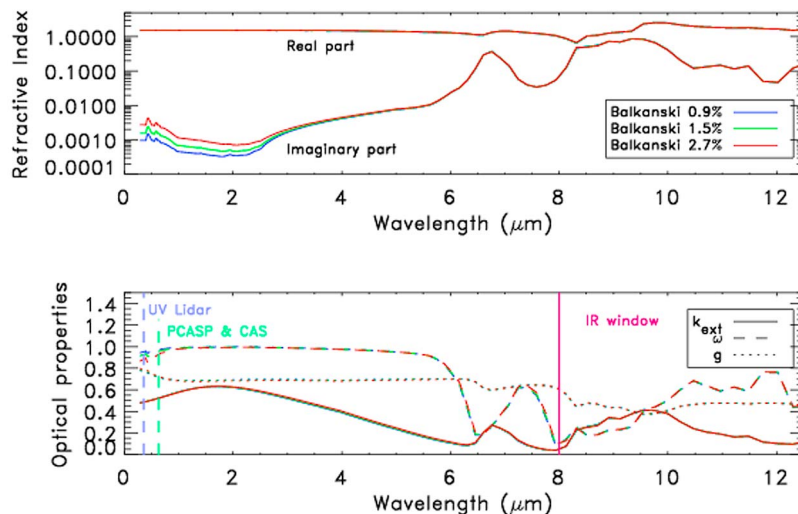


**Figure 1.** Refractive index and optical properties as a function of wavelength ( $\lambda$ , in  $\mu\text{m}$ ) based on Mie-Lorenz theory including normalized extinction ( $k_{\text{ext}}(\lambda) / k_{\text{ext}}(\lambda = 355 \text{ nm})$ ), single scattering albedo ( $\omega$ ), and asymmetry parameter ( $g$ ). All radiative transfer modeling in this paper assumes the 1.5% hematite level of *Balkanski et al.* [2007] (green curves in upper plot; blue and red represent 0.9% and 2.7% hematite respectively). Wavelengths corresponding to the lidar, PCASP/CAS and infrared window measurements are shown in the lower plot as vertical bars. The optical properties shown here have been calculated assuming the irregular particle model in the CAS data analysis.

aircraft on 17 May 2010 [*Schumann et al.*, 2011] for which the coarse mode size distribution is broader than the FAAM data and peaks at larger sizes. *Turnbull et al.* [2012] present fitted PSDs for these different choices; in the present work we consider three cases:

[19] FAAM (A) The default assumption, using a PSD derived from CAS data assuming irregular (polyhedral) particles for the coarse mode and applying Mie-Lorenz theory to derive infrared optical properties replacing polyhedrals with equivalent volume spheres.

[20] FAAM (B) As for FAAM (A) except that spheres are assumed throughout including in the CAS data analysis. This results in an increased geometric mean diameter of  $4.0 \mu\text{m}$ , compared to  $3.6 \mu\text{m}$  for FAAM (A), and increased standard deviation of the lognormal distribution (1.85 c.f. 1.8). Overall this leads to a strengthening of infrared extinction relative to shortwave ( $0.55 \mu\text{m}$ ) extinction by approximately 10% (at  $10 \mu\text{m}$ ) to 19% (at  $12.5 \mu\text{m}$ ) compared with the irregular model.

[21] DLR This case assumes spheres but replaces the CAS-derived PSD with lognormal fits based on DLR airborne data. The coarse mode has a geometric mean diameter of  $9.6 \mu\text{m}$  and standard deviation of 2.5. This strengthens the infrared to shortwave extinction ratio by approximately 35% ( $10 \mu\text{m}$ ) to 134% ( $12.5 \mu\text{m}$ ) compared with FAAM (A).

[22] FAAM cases (A) and (B) incorporate the refractive index of *Balkanski et al.* [2007], with a 1.5% hematite content, for the coarse mode and a refractive index appropriate for sulphuric acid for the fine mode: these are required for the interpretation of CAS (680 nm), PCASP (630 nm) and lidar (355 nm) data. This implies a refractive index of  $1.52 + 0.0015i$  (coarse mode) and  $1.43 + 0.00i$  (fine mode) which is specified across all UV-visible wavelengths.

[23] For the DLR case we follow *Schumann et al.* [2011] who used a refractive index of  $1.59 + 0.004i$  (at 632 nm)

as a best estimate for deriving PSDs from their optical particle counter data in a uniform analysis of 33 different plume penetrations. They found high variability and size dependence of the refractive index. Larger particles were less absorbing than smaller ones and the refractive index varied during different plume encounters. An imaginary refractive index of 0.008 implied particle sizes larger than observed on particle impactors and larger than expected due to particle sedimentation. Zero absorption could be another reasonable assumption in deriving particle sizes. It is important to recognize that we still use the *Balkanski et al.* [2007] refractive index for the generation of optical properties at *all other wavelengths* using Mie-Lorenz theory. The parameters used for the three cases are summarized in Table 1.

[24] Note that even with our use of an irregular model to derive a representative PSD from CAS data for the FAAM (A) case we still assume spheres when applying Mie-Lorenz theory to calculate optical properties over an extended spectral range. In order to justify the use of Mie-Lorenz calculations in this work the scalar optical properties (i.e., extinction cross section,  $\omega_0$  and  $g$ ) calculated assuming equal volume spheres have been compared against exact T-matrix [*Havemann and Baran*, 2001] calculations assuming randomly oriented hexagonal columns of aspect ratio unity (ratio of length-to-diameter) at three wavelengths. The three wavelengths were  $8.2 \mu\text{m}$ ,  $9.8 \mu\text{m}$  and  $11.0 \mu\text{m}$ , with complex refractive indices of  $0.792 + 0.255i$ ,  $2.537 + 0.631i$ , and  $1.825 + 0.143i$ , respectively [*Balkanski et al.*, 2007]. The calculations at the three wavelengths were performed using three size bins from the representative PSD measured by Johnson et al. (submitted manuscript, 2011), which were  $11.62 \mu\text{m}$ ,  $23.55 \mu\text{m}$ , and  $33.52 \mu\text{m}$ . The results of comparing the Mie-Lorenz calculations against T-matrix show that the extinction cross section,  $\omega_0$  and  $g$  are generally within

**Table 1.** Parameters Used in the Derivation of Optical Properties for Three Cases Labeled as FAAM (A), FAAM (B) and DLR<sup>a</sup>

	FAAM Irregulars (A)		FAAM Spheres (B)		DLR Case	
	Fine Mode	Coarse Mode	Fine Mode	Coarse Mode	Fine Mode	Coarse Mode
Shape	sphere	irregular	sphere	sphere	sphere	sphere
Re(RI)	1.43	1.52	1.43	1.52	1.59	1.59
Im(RI)	0.00i	0.0015i	0.00i	0.0015i	0.004i	0.004i
$D_g$	0.20	3.6	0.20	4.0	0.12	9.6
$\sigma$	1.4	1.8	1.4	1.85	1.6	2.5

<sup>a</sup>The PSDs are represented by one fine mode and one coarse mode and are fitted to lognormal functions with parameters  $D_g$  (geometric mean diameter, in  $\mu\text{m}$ ) and  $\sigma$  (standard deviation). The fits are to PCASP-100X and CAS data (fine mode and coarse mode respectively) for FAAM cases (A) and (B) whereas for the DLR case the fit is to data from PCASP-100X and FSSP-300 probes on the Falcon aircraft [Schumann *et al.*, 2011]. Re(RI) and Im(RI) denote the real and imaginary parts of the complex refractive index assumed at UV-visible wavelengths for the calculation of scalar optical properties. For further details, see Turnbull *et al.* [2012, Table 2] and associated discussion.

10%, 2% and <1% respectively of the exact calculations. Given that the lidar-derived aerosol extinction and ash mass concentration have estimated uncertainties of 30% and 100% respectively, errors of less than 10% in calculating the scalar optical properties are not considered significant for the purposes of this paper. Moreover, it has been demonstrated by Yang *et al.* [2007] that the nonsphericity effect of dust particles is not significant at thermal infrared wavelengths.

#### 2.4. Radiative Transfer Modeling

[25] We apply the optical properties described in section 2.3, calculated using Mie-Lorenz theory, to full scattering calculations covering the range of wavelengths to which the FAAM BAe-146 remote sensing instrumentation is sensitive. We distinguish between the shortwave solar spectrum and the thermal infrared region. For the shortwave data analysis we perform model calculations using the flexible *Edwards and Slingo* [1996] radiation code with 220 bands in the solar spectral region. The two-stream radiative transfer calculations account for the scattering and absorption by gaseous components. Profiles of water vapor and temperature are taken from a dropsonde released in the vicinity of the highest observed ash concentrations over the southern North Sea, while concentrations of carbon dioxide, oxygen, nitrous oxide, methane and ozone are set to climatological values. Above the level of the aircraft, the climatological concentrations from McClatchey *et al.* [1972] for a midlatitude summer atmosphere are assumed for water vapor and ozone. The spectrally dependent sea-surface reflectance is assumed to be that of Cox and Munk [1954] using a 10 m wind speed of  $3.2 \text{ ms}^{-1}$  as measured by dropsonde. The solar constant is calculated from standard solar geometry to be  $1335.1 \text{ W m}^{-2}$  and variations in the solar zenith angle are included. Volcanic ash aerosol is specified using the bi-modal lognormal size distributions defined in Table 1. Applying Mie-Lorenz scattering theory these measurements and assumptions yield a specific extinction coefficient,  $k_{ext}$ , of  $0.50 \text{ m}^2 \text{ g}^{-1}$ , a single scattering albedo,  $\omega_0$ , of 0.95, and an asymmetry parameter,  $g$ , of 0.70 at a wavelength of  $0.55 \mu\text{m}$ . The vertical profile of volcanic ash is assumed to be represented by the lidar extinction observations.

[26] The Havemann-Taylor Fast Radiative Transfer Code (HTFRTC) has been developed at the Met Office as a fast forward model and 1-dimensional variational inverse model. We use HTFRTC for modeling radiances over the mid-infrared spectral range. The use of principal components as a basis in HTFRTC, in contrast to line-by-line calculations,

permits accurate and efficient computation [Liu *et al.*, 2006; Havemann, 2006]. More recently, scattering has been incorporated which allows the simulation of cloud and aerosol scenes as well as clear sky profiles [Havemann *et al.*, 2009]. In the case of aerosols the code requires the key spectral properties of normalized extinction cross section  $\sigma$ , single scattering albedo  $\omega_0$  and asymmetry parameter  $g$  (we use the same set of Mie-Lorenz calculations as included in the Edwards-Slingo shortwave calculations but extended to longer wavelength). Similarly to the Edwards-Slingo model, the scattering code contained within HTFRTC computes the diffuse radiances by decomposing the radiance field into spherical harmonics in order to calculate the scattered component of the reflected radiances, which are then integrated along a ray following the scheme proposed by Benassi *et al.* [1984]. A fuller description is given by Ringer *et al.* [2003]. We initialize HTFRTC with profiles of temperature and humidity from dropsonde observations, an ozone concentration profile from FAAM BAe-146 in situ measurements and vertical extinction profiles from the airborne lidar. Trace gases other than ozone are represented as climatological profiles. HTFRTC does not currently include absorption due to  $\text{SO}_2$  which we neglect for the reasons discussed in section 3.2. We also require an estimate of sea surface temperature (SST) which we choose for consistency with ARIES downward-looking radiances at the lowest available altitude over the southern North Sea (284.0 K). For sea surface emissivity we use the spectrally varying emissivity of Newman *et al.* [2005] valid at 287 K.

### 3. Aircraft Remote Sensing Measurements

#### 3.1. Shortwave Irradiance Observations

[27] The FAAM aircraft was fitted with broadband and spectrally resolved shortwave radiometers during the Eyjafjallajökull eruption. These included upward- and downward-looking clear-domed and red-domed Eppley broadband radiometers (BBRs) covering the spectral ranges  $0.3\text{--}3.0 \mu\text{m}$  and  $0.7\text{--}3.0 \mu\text{m}$  respectively, instrumentation that has previously been used to detect the radiative effect of mineral dust off the coast of West Africa [e.g., Haywood *et al.*, 2003, 2011]. The BBRs are installed at a nominal  $3^\circ$  pitched forward angle to the airframe to account for the pitch of the aircraft when under standard operating conditions. The Short-wave Hemispherical Integrating Measurement System (SHIMS) uses two temperature-controlled Carl Zeiss

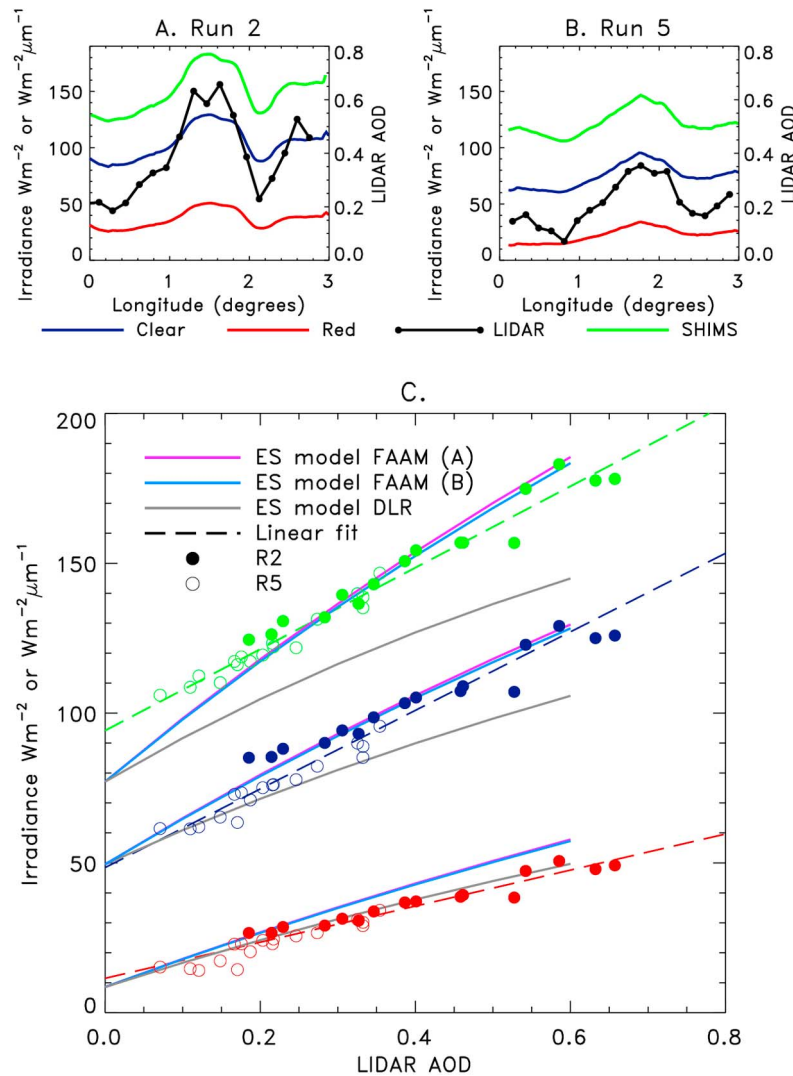


**Figure 2.** (a) Variation in clear dome (blue line) and red dome (red line) broadband upwelling fluxes and lower (downward-pointing) SHIMS  $0.55 \mu\text{m}$  irradiance (green line) along Run 2 of FAAM BAe 146 flight on 17 May 2010 over the North Sea. Run 2 was performed at an altitude of 8.5 km with data shown between the times 14:19–14:37 UTC. Also shown for comparison (connected black dots) is the lidar-derived AOD for the run. (b) As in Figure 2a, data shown for Run 5 at 8.2 km altitude between the times 15:38–15:58 UTC. Runs 2 and 5 were oriented west-east along  $54.0^\circ\text{N}$  and  $54.5^\circ\text{N}$  respectively. (c) Relationship between irradiances and lidar AOD. Data for the clear dome (blue), red dome (red), and SHIMS at  $0.55 \mu\text{m}$  (green) are shown for Run 2 (filled circles) and Run 5 (open circles). Linear fits to the data result in the dashed lines shown. Simulated irradiances using the Edwards-Slingo model are plotted as solid lines for FAAM (A) case in purple, FAAM (B) case in blue and DLR case in gray.

spectrometer modules operating in the spectral range  $0.30\text{--}0.95 \mu\text{m}$  and  $0.95\text{--}1.70 \mu\text{m}$ . The pixel separation is approximately  $0.0033 \mu\text{m}$  in the  $0.30\text{--}0.95 \mu\text{m}$  module and  $0.006 \mu\text{m}$  in the  $0.95\text{--}1.70 \mu\text{m}$  module, giving approximate spectral resolutions of  $0.010 \mu\text{m}$  and  $0.018 \mu\text{m}$  with an in-house designed integrating head. The SHIMS instrument provides counts per millisecond; during this measurement campaign the data were not fully calibrated so we use model radiative transfer data to calibrate the modules as described below.

### 3.1.1. Broadband Irradiances

[28] Figure 2 shows results from two high altitude (between 8 and 9 km) runs above the ash layer, comparing

the response of the BBR and SHIMS ( $0.55 \mu\text{m}$  single wavelength) irradiances along the run with simultaneous lidar derived aerosol optical depth (AOD) [Marengo *et al.*, 2011]. The data clearly show similar trends, with a peak in signal between  $1$  and  $2^\circ\text{E}$  for both runs. The difference between the two runs (lower AOD and BBR signal during Run 5) is likely due to Run 5 being positioned further north than Run 2, and at a later time, as the ash moved south. Figure 2c compares model results with the observed relationship between BBR irradiances and lidar AOD. We consider the three sets of optical properties described in section 2.3: FAAM (A), FAAM (B) and DLR. There is very

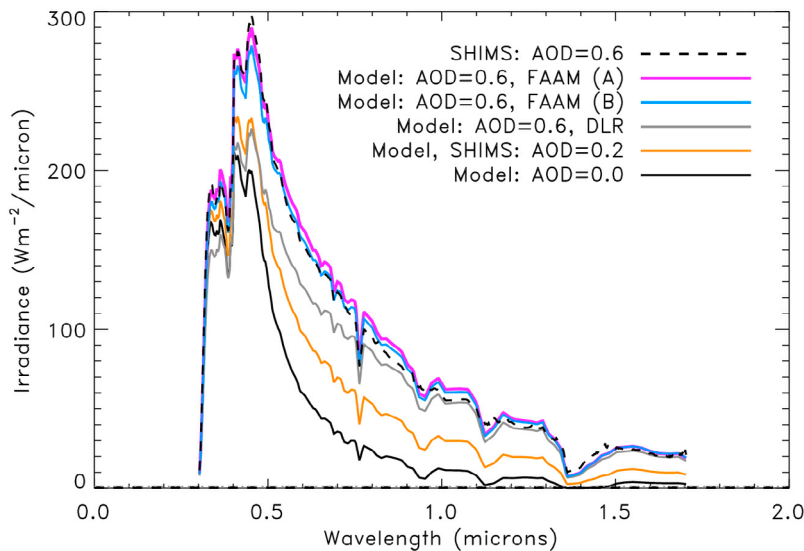


**Figure 3.** Spectral variation in the upwelling irradiance ( $\text{Wm}^{-2}/\mu\text{m}$ ): model spectral irradiance when  $\text{AOD} = 0$  (black solid line), model and measured spectral irradiance when  $\text{AOD} = 0.2$  (orange line), and measured (black dashed line) when  $\text{AOD} = 0.6$ . Also shown are modeled irradiances for  $\text{AOD} = 0.6$ : FAAM (A) case for irregular particles (purple line), FAAM (B) case for spheres (blue line), DLR case (gray line).

little difference between the FAAM (A) and FAAM (B) calculations, indicating that the modeled shortwave irradiances are not particularly sensitive to assumptions of particle shape. There are major differences, however, between the FAAM cases and DLR case: using the DLR size distribution results in significantly lower calculated irradiances. Although the DLR calculations are in reasonable agreement with the red dome BBR irradiances, agreement is poor for the clear dome and SHIMS measurements. With FAAM cases (A) and (B) the model reproduces the observed signal well, particularly for the clear dome irradiance, over a range of AOD between 0.1 and 0.7.

[29] The linear-fit slopes of Figure 2c yield the instantaneous radiative forcing efficiency. Over the  $0.3\text{--}3.0\ \mu\text{m}$  (clear dome) region the intercept is  $48 \pm 5\ \text{Wm}^{-2}$  (following the error analysis of Haywood *et al.* [2010]) which is in agreement with the model calculations when aerosol is excluded. The radiative forcing efficiency from the slope is  $-130 \pm 5\ \text{Wm}^{-2}/\tau$  (minus sign adopted for consistency with Intergovernmental Panel on Climate Change [2007]) where  $\tau$  is the  $0.55\ \mu\text{m}$  AOD. This value is very similar to that derived for Saharan dust during the GERBILS campaign where a radiative forcing efficiency of  $-127\ \text{Wm}^{-2}/\tau$  was measured for similar solar zenith angles. Given the dominance of the coarse mode particles in both volcanic ash and mineral dust, and the similar assumptions about the refractive indices, this agreement is perhaps not surprising. The agreement of radiative transfer calculations with observations is indicative that the underlying assumptions of aerosol size distribution, complex refractive index and particle shape are sufficiently robust for modeling the aerosol scattering properties across the shortwave spectrum.

### 3.1.2. SHIMS Spectral Irradiances

[30] In addition to the broadband irradiances available from the BBRs, the SHIMS instrument is capable of investigating the spectral dependence of the irradiances. As a

robust calibration methodology for the SHIMS instrument has yet to be developed, we use model calculations when the AOD at  $0.55\ \mu\text{m}$  is at a minimum of around 0.2 at approximately  $0.3^\circ$  longitude along Run 2 (Figure 2a). The modeled and predicted spectral irradiances are then compared to provide a calibration factor that relates the counts/ms recorded by SHIMS to  $\text{Wm}^{-2}/\mu\text{m}$ . Haywood *et al.* [2001] applied this method to Saharan dust off the coast of West Africa and were able to demonstrate ‘radiative closure’. That campaign had the advantage of observing upwelling fluxes over regions with very low turbidity which could be robustly used for calibration of the SHIMS instrument. Here, the use of spectral irradiances when a significant AOD is present is not ideal for calibration owing to the associated inherent uncertainties, but it is the most tractable method available. The SHIMS irradiance at  $0.55\ \mu\text{m}$  is shown on each of the panels of Figure 2, exhibiting the same characteristics as the BBRs. The slope shown in Figure 2c is statistically identical to that of the clear domed BBR at  $131 \pm 5\ \text{Wm}^{-2}/\mu\text{m}/\text{AOD}$  indicating that the  $0.55\ \mu\text{m}$  wavelength can usefully be used to approximate the broadband direct radiative effect.

[31] Figure 3 shows the modeled and measured spectral irradiance for an AOD of 0.0, 0.2, and 0.6. The  $\text{AOD} = 0.6$  measurements are an average from  $1.3$  to  $1.7^\circ$  longitude along Run 2 as shown in Figure 2a. The calibration procedure means that the modeled and measured spectral irradiances are identical when  $\text{AOD} = 0.2$ . When the AOD reaches 0.6, there is a significant increase in the reflected irradiance in both the modeled and measured spectral irradiances. The modeled irradiance for  $\text{AOD} = 0.6$  using the DLR optical properties is generally too low to reproduce the SHIMS measurements, particularly at shorter wavelengths. The FAAM (A) and (B) optical properties achieve a better fit, with the agreement between model and observations showing that the spectral dependence of the optical properties at wavelengths throughout the  $0.3\text{--}1.7\ \mu\text{m}$  range is well

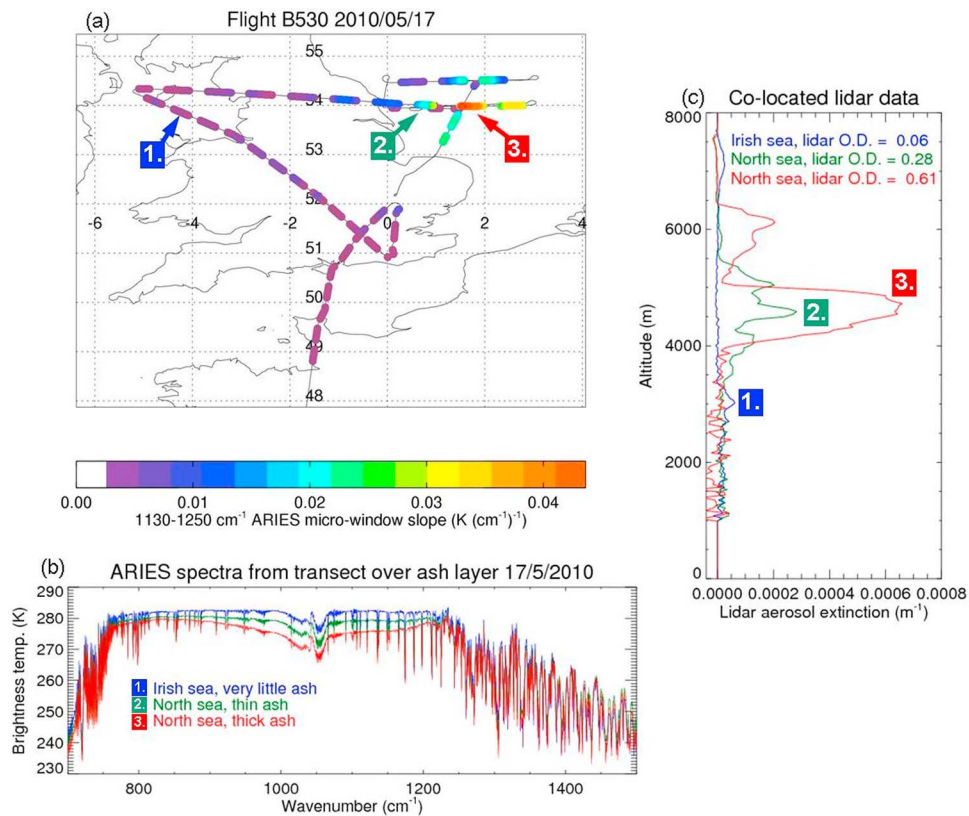


**Figure 4.** (a) Flight track of the FAAM BAe 146 aircraft on 17 May 2010. The track is overlaid with color-coded ARIES observations of the brightness temperature slope for micro-windows in the range  $1130\text{--}1250\text{ cm}^{-1}$ . The labels 1, 2, 3 denote the locations of representative low, medium and high ash loadings respectively. (b) ARIES downward-looking brightness temperature spectra for the three selected locations above the ash layer, spanning the mid-infrared atmospheric window region. (c) Lidar extinction profiles collocated with the three selected ARIES observations, with total AOD in the range 0.06 to 0.61 (see legend).

captured. Indeed, the agreement at wavelengths exceeding  $0.55\text{ }\mu\text{m}$  is better than that determined by *Haywood et al.* [2011] when investigating Saharan dust suggesting an accurate representation of the coarse mode. Again this suggests that the optical properties are well characterized giving further confidence in the measurements of the size distribution and the choice of refractive index [*Turnbull et al.*, 2012; Johnson et al., submitted manuscript, 2011].

### 3.2. ARIES Infrared Radiances

[32] The Airborne Research Interferometer Evaluation System [*Wilson et al.*, 1999] is a modified Bomem MR200 interferometer, measuring infrared radiances over two spectral bands between  $550\text{--}3000\text{ cm}^{-1}$  ( $18\text{--}3.3\text{ }\mu\text{m}$ ) at  $1\text{ cm}^{-1}$  resolution. It is capable of scanning vertically upwards and a number of view angles cross-track downward. The data analysis presented here is applied mainly to views directly downward during high-altitude aircraft runs above the volcanic ash layer(s); we also briefly consider views directly upwards during runs beneath the ash.

[33] The infrared spectrum is particularly sensitive to the presence of ash in the window region between approximately  $770\text{--}1250\text{ cm}^{-1}$ . A number of authors have suggested schemes for using brightness temperature signatures for ash detection from space [e.g., *Gangale et al.*, 2010;

*Clarisse et al.*, 2010b]. Analysis of ARIES spectra recorded during the Eyjafjallajökull eruption episode in April/May 2010 showed a very straightforward correlation between the brightness temperature slope in micro-windows between  $1130\text{--}1250\text{ cm}^{-1}$  and the presence of ash in the field of view. (By micro-windows we mean ARIES spectral channels with a clear sky transmittance close to unity.) Note that this spectral slope method is very similar in practice to calculating a brightness temperature difference for two channels, such as for  $1231.5$  and  $1168\text{ cm}^{-1}$  described by *Clarisse et al.* [2010b], although the calculation of a slope using multiple channels does assist in reducing the impact of instrument noise for any particular channel. *Clarisse et al.* demonstrated even better performance for a spectral shape correlation method, particularly for the discrimination of ash from desert dust; however, we find for this case study that the spectral slope gives adequate information for ARIES ash detection.

[34] The derived brightness temperature slope for ARIES data collected on 17 May 2010 is shown in Figure 4a. For the early part of the flight over southern England and the Irish Sea the slope is consistently close to zero, despite considerable variations in the expected infrared surface emissivity and variable cloud amounts detected by the lidar. This finding gives confidence that the simple slope diagnostic is not

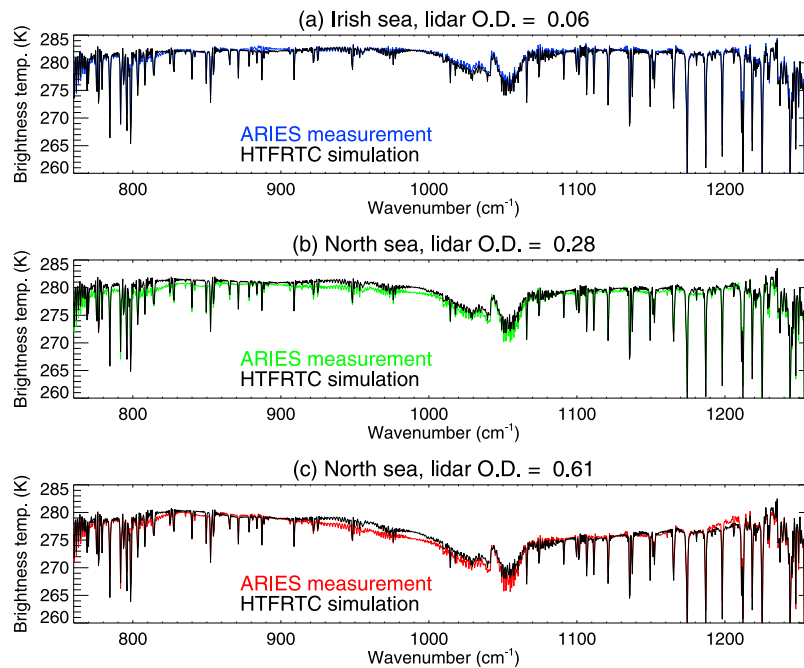


**Figure 5.** ARIES measured brightness temperatures overlaid with HTFRTC simulations for three examples of ash optical thickness in the down-looking scene (see Figure 4). The collocated lidar extinction profile has been used as input to the HTFRTC simulation in each case. (a) Lidar AOD of 0.06; (b) AOD of 0.28; (c) AOD of 0.61. Calculations are for the FAAM (A) set of optical properties.

overly prone to false-positive identifications of ash. The later part of the flight over the North Sea encountered much higher aerosol concentrations (as detected by the lidar) with a concomitant increase in the ARIES slope diagnostic. The position of the maximum ash detection values correlates well with other observations of the peak plume concentrations [see, e.g., *Turnbull et al.*, 2012, Figure 3].

[35] For ease of analysis a subset of the data has been selected based on lidar inferred AOD values. AODs are calculated from the altitude below which the identified ash signature is negligible up to the aircraft altitude. Figure 4a shows three subset locations corresponding to (1) very low AOD over the Irish Sea, (2) intermediate AOD close to the coast over the southern North Sea, and (3) high AOD further east over the southern North Sea. The respective ARIES brightness temperatures and lidar extinction profiles for these locations are shown in Figures 4b and 4c. The ARIES brightness temperature depression in the 770–1250  $\text{cm}^{-1}$  range due to the presence of ash is clearly observed. The sample locations were carefully selected to be free of cloud based on examination of lidar backscatter returns.

[36] Figure 5 shows the results of HTFRTC simulations across the mid-infrared window region, taking as input the dropsonde-measured atmospheric temperature and humidity profile and the collocated lidar aerosol extinction profile for each of the three test locations, compared with ARIES observations. The FAAM (A) (i.e., irregular model) optical properties have been used in the simulations. A number of features are common to all three spectra, such as numerous water vapor emission lines and the ozone band centered at 1050  $\text{cm}^{-1}$ . The impact of ozone on the ARIES spectrum is relatively small compared to IASI (see section 4) since the FAAM aircraft was flying at an altitude of approximately

8 km, below the majority of the ozone column concentrated in the stratosphere. The aerosol signal is seen as a broad depression in brightness temperature with maximum impact around 1000–1100  $\text{cm}^{-1}$ . The agreement of simulations with measurements is generally good over the range of AOD studied here, with the magnitude and spectral shape of the aerosol signature captured well. We ascribe the good match of Mie-Lorenz calculations to the measurements partly to the highly absorbing nature of mineral dust in the mid-infrared region and the ash plume being composed of small particles. This gives confidence that optical properties such as these can be used to derive quantitative estimates of ash loading from hyperspectral satellite instruments. Results of retrievals using IASI observations are presented in section 4.

[37] The results shown in Figures 4 and 5 suggest that there is a predictable relationship between the ARIES brightness temperature signal and the associated lidar AOD. Each of 80 lidar observations (1 min averages) are compared with the ARIES 1130–1250  $\text{cm}^{-1}$  slope for collocated data in Figure 6a; additionally, HTFRTC simulations have been performed for each lidar extinction profile, and the synthetic brightness temperature slope computed. Calculations for an idealized aerosol layer at an average height of 2.5, 5.0 and 10.0 km are also shown, extended to greater range in AOD in Figure 6b. Several conclusions can be drawn from Figure 6. First, there is a clear trend of increasing ARIES slope diagnostic with lidar AOD, which shows that the measured brightness temperatures are sensitive to the underlying ash for AODs greater than approximately 0.2. (Or, conversely, ARIES is recording an unambiguous ash signal where the slope diagnostic is around 0.01  $\text{K}(\text{cm}^{-1})^{-1}$  or higher.) We note that for very low AOD values the brightness temperature spectrum is significantly dependent

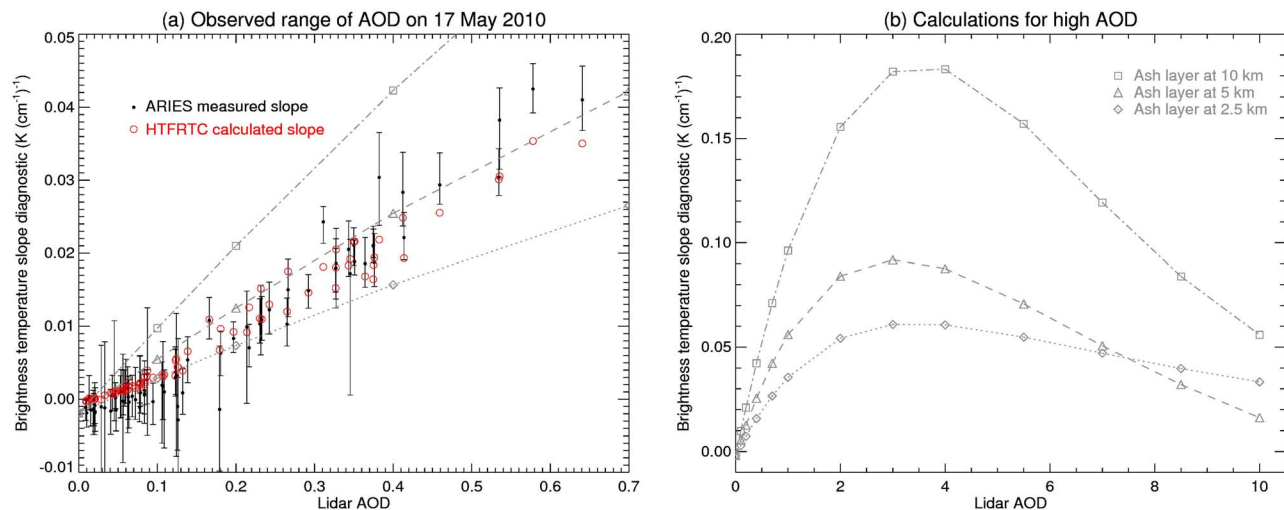


**Figure 6.** Relationship between ARIES micro-window brightness temperature slope diagnostic and lidar AOD. (a) Observations on 17 May 2010: ARIES data have been aggregated over 1 min intervals corresponding to the collocated lidar observations, and the 1130–1250 cm<sup>-1</sup> slope is plotted as solid data points with minimum and maximum values within each time interval as bounding bars. HTFRTC simulations are used to simulate the micro-window slope for each of the lidar extinction profiles (open circles in red). Also shown are calculations based on idealized vertical extinction profiles with the aerosol lying uniformly in the range 1.75–3.25 km (diamonds, dotted line), 4.25–5.75 km (triangles, dashed line) and 9.25–10.75 km (squares, dot-dash line). (b) Idealized calculations as in Figure 6a, presented for a larger range of AOD.

on the underlying surface observed through the ash which may be land, or cloud, with variable spectral emissivity. Second, the relationship between ARIES slope and lidar AOD is dependent on the height of the ash, since aerosol at a higher altitude will present a greater temperature contrast (and hence a greater brightness temperature signal) between the ash layer and the surface. The thickest ash layers observed by the lidar over the North Sea occurred at an altitude of between 4.5–6.0 km. By contrast, during the earlier part of the flight (over the Irish Sea and UK mainland) a much thinner ash layer was observed at an altitude of 3.0–3.5 km. The HTFRTC simulated slopes reflect this: departures from a straight line relationship versus AOD are caused by variations in the height of the ash. Third, the HTFRTC simulations are in good agreement (c.f. Figure 5) with ARIES measurements over a range in AOD up to 0.64, which gives confidence in the appropriateness of the ash optical properties used in HTFRTC for this case. At higher optical depths, Figure 6b, the calculations show that the approximately linear relationship between brightness temperature signal and AOD breaks down. For AOD values of 1 or greater the ash layer behaves more like an opaque blackbody, with an asymptotic limit of zero for the micro-window slope at very high AOD. Importantly, the IASI ash retrieval algorithm we discuss in section 5, based on an optimal estimation approach rather than simply brightness temperature channel differences or slopes, behaves robustly in situations of low to high aerosol loadings.

[38] *Turnbull et al.* [2012] describe how FAAM in situ measurements of SO<sub>2</sub> concentrations were well correlated with ash mass loadings on 17 May 2010. The peak SO<sub>2</sub> concentration encountered was 46 nmol mol<sup>-1</sup> while the peak columnar density was 4.5 Dobson units. SO<sub>2</sub> exhibits infrared absorption bands in the ranges 1080–1220 cm<sup>-1</sup>

and 1320–1400 cm<sup>-1</sup> which enable its detection from space [*Clarisse et al.*, 2008]. In order to test the impact of SO<sub>2</sub> absorption on ARIES spectra, the Line-By-Line Radiative Transfer Model (LBLRTM) [*Clough et al.*, 2005] has been used to simulate the brightness temperature impact of the highest observed SO<sub>2</sub> vertical profile. We find that over the 1080–1220 cm<sup>-1</sup> spectral range the change in brightness temperature due to SO<sub>2</sub> is no more than 0.2 K. Between 1320 and 1400 cm<sup>-1</sup> a greater impact of up to 1.4 K is modeled. Importantly, the effect on derived ARIES slope in the 1130–1250 cm<sup>-1</sup> range for the cases we consider here is rather small (approximately 3%).

[39] It is worth noting also that the ash spectral signature depends on the specific composition (and therefore aerosol complex refractive index) and grain size as documented for a number of volcanic eruptions by *Clarisse et al.* [2010b]. The impact of differing refractive indices on ash retrievals from infrared spectra is discussed further in section 4.

[40] As illustrated by Figure 5, we obtain good agreement between ARIES brightness temperatures and simulations where we use collocated lidar extinction profiles and optical properties based on irregular particles. We now assess the sensitivity of the simulations to assumptions of particle shape and size by testing against ARIES observations the three sets of optical properties summarized in Table 1.

[41] We select ARIES spectra matched to coincident lidar observations where the derived AOD exceeded 0.4 (the maximum AOD encountered was 0.64). In this way we sample the set of ARIES spectra for which we have greatest sensitivity to the aerosol signature. Figure 7 compares HTFRTC simulations with ARIES spectra using as input the collocated lidar profiles. The mean and standard deviation of the observed-calculated residuals are shown for different choices of optical properties in Figures 7b–7d; we exclude

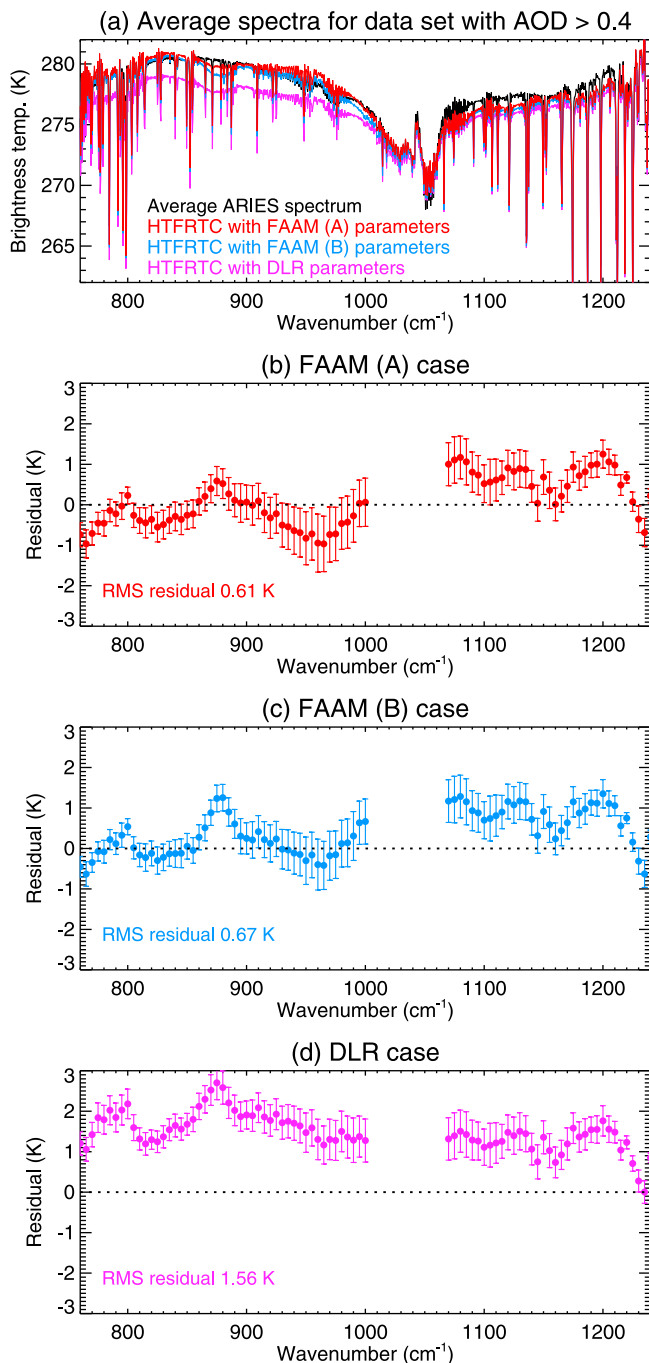


**Figure 7.** (a) Average ARIES brightness temperature spectrum (black) across the infrared window region 760–1240  $\text{cm}^{-1}$  (13.2–8.1  $\mu\text{m}$ ) where data have been collocated with lidar AODs in the range greater than 0.4. Also plotted are average HTFRTC simulations with three sets of optical properties, as described in the text: FAAM (A) in red, FAAM (B) in blue, DLR in purple. (b–d) Observed-calculated brightness temperature residuals for each set of optical properties, where simulations have been performed for each coincident lidar profile and the mean (solid circles) and standard deviation (error bars) of the residuals calculated for the subset of ARIES spectra.

the spectral region near 1050  $\text{cm}^{-1}$  as here the ozone absorption interferes with the aerosol signal. The irregular model FAAM (A) and spherical model FAAM (B) produce the smallest brightness temperature residuals which are generally within  $\pm 1.5$  K. By contrast, assuming spherical particles and the DLR PSD gives larger positive residuals in excess of 2 K.

[42] Across the spectral interval shown in Figure 7 the root mean square (RMS) residuals are 0.61 K, 0.67 K and 1.56 K for FAAM (A), FAAM (B) and DLR cases respectively. There is considerable spectral variation: in particular, all three sets of optical properties produce a local peak in the residuals at 875  $\text{cm}^{-1}$  which appears to be related to features in the data of *Balkanski et al.* [2007] at this frequency. Given that the refractive index is valid for desert dust rather than volcanic ash it is perhaps not surprising that the calculated radiances are not a perfect match to the observations. Indeed, the overall agreement is very good considering the various uncertainties in refractive index, optical particle counter PSDs and lidar extinction profiles.

[43] The results in Figure 7 serve to emphasize the importance of adequately specifying the PSD applied to Mie-Lorenz calculations. The residuals in Figure 7d for the DLR case are consistently positive due to the increased ratio of longwave to shortwave extinction, which results from a much broader PSD with higher geometric mean diameter than the FAAM data. The choice of spheres or irregular particles in the analysis, by contrast, does not dramatically affect the extinction across the wave number range studied here.

[44] It is instructive to model the impact of differing assumptions of complex refractive index. Taking the FAAM (A) PSD as default, we simulate the high AOD cases as before; this time we generate optical properties based on the refractive index of mineral dust [*Balkanski et al.*, 2007], and volcanic materials andesite and obsidian (both tabulated by *Pollack et al.* [1973]). Obs-calc residuals for ARIES using the three data sets are shown in Figure 8. Not only are the RMS residuals significantly smaller when using the refractive indices of *Balkanski et al.* [2007] compared to the other choices, the spectral shape of the ash signature is markedly different for the various refractive indices. Optical properties based on andesite and obsidian are a poor fit to the ARIES observations, leading to residuals of 3–4 K at some frequencies.

[45] When flying above the ash ARIES is mimicking the nadir-viewing geometry of a satellite instrument such as IASI. However, ARIES also has the capability to view upwards, and by flying underneath the ash layer on 17 May 2010 we obtained measurements of the downwelling radiance. This allows the radiative transfer to be tested in conditions where there may be a different balance between absorption/emission and scattering into the field of view. One complication with analyzing the downwelling data is the lack of collocated aerosol extinction data (since the FAAM lidar is only downward-looking). It is only possible therefore to test the qualitative agreement of radiative transfer calculations with the measurement, for an estimated extinction profile.

[46] Figure 9 shows the average ARIES downwelling radiance recorded below the ash layer present over the North Sea on 17 May 2010. As in the upwelling spectra (see

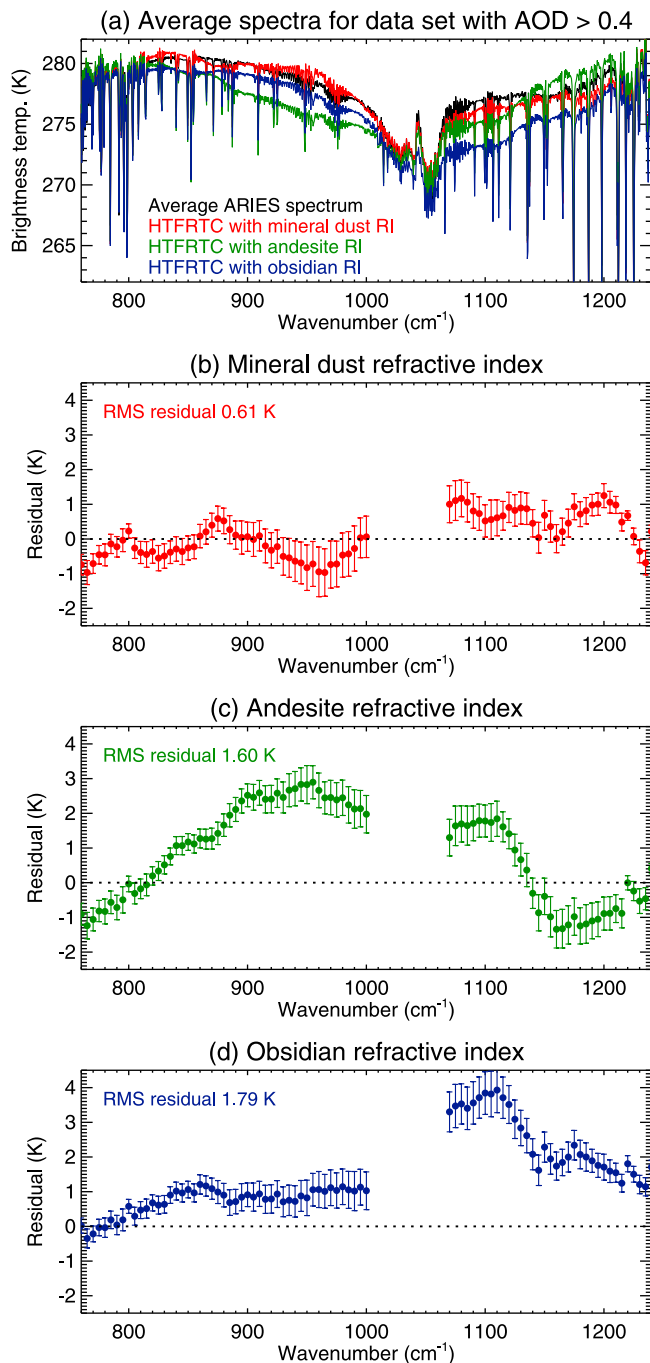


**Figure 8.** (a) Average ARIES brightness temperature spectrum (black) as shown in Figure 7. Also plotted are HTFRTC simulations based on different assumed refractive indices: mineral dust [Balkanski *et al.*, 2007] in red; andesite [Pollack *et al.*, 1973] in green; obsidian [Pollack *et al.*, 1973] in blue. (b–d) Observed-calculated brightness temperature residuals for each refractive index data set. The FAAM (A) PSD has been used to generate the optical properties for HTFRTC.

Figure 5) the peak aerosol signal, corresponding to an increase in downwelling radiance, coincides with the position of the ozone band near  $1050\text{ cm}^{-1}$ . An HTFRTC simulation has been run with the average lidar vertical profile of

extinction, but scaled by a factor to match the observed radiance signal. Thus the extinction profile used gives an effective AOD of 0.33. We emphasize that although the simulation has been constrained to match the magnitude of the ARIES radiance, the spectral shape is entirely determined by the aerosol optical properties used in HTFRTC. The good match in Figure 9 is therefore further corroboration of the aerosol size distribution, complex-refractive index and Mie-Lorenz calculations which have been used to derive the infrared optical properties.

[47] Note that we have restricted ourselves here to the infrared window around  $760\text{--}1240\text{ cm}^{-1}$  (approximately  $13\text{--}8\text{ }\mu\text{m}$ ). The ARIES spectra extend to  $3000\text{ cm}^{-1}$  ( $3.3\text{ }\mu\text{m}$ ) maintaining reasonable signal-to-noise and in principle provide additional information with which to test our set of optical properties. However, the combination of solar scattering at shorter wavelengths in addition to the thermal radiative transfer makes this spectral region more challenging to study. We intend to extend our analysis to the  $3\text{--}4\text{ }\mu\text{m}$  region in a future publication.

#### 4. IASI Observations and Retrievals

[48] The Infrared Atmospheric Sounding Interferometer (IASI) is a high resolution infrared sounder onboard Metop-A which measures the Earth's outgoing radiation twice a day globally with a  $12\text{ km}$  diameter footprint at nadir. The spectrometer has a wide spectral coverage  $645\text{--}2760\text{ cm}^{-1}$  with a medium to high spectral resolution ( $0.5\text{ cm}^{-1}$  apodized, sampled at  $0.25\text{ cm}^{-1}$ ) [Clerbaux *et al.*, 2009].

[49] Recently, a radiative transfer code was proposed for the retrieval of trace gases and aerosols from observed spectra [Clarisse *et al.*, 2010a] of which the most important aspects are summarized here. Its forward model is based on a spherical layer model of the atmosphere and uses a doubling-adding routine (supporting an arbitrary number of streams) to deal with the effects of multiple scattering on aerosols. The retrieval is based on the optimal estimation approach, and can be used to simultaneously retrieve both trace gas concentrations and aerosol loadings and effective radii. Unlike other codes, it does not rely on two step retrievals, lookup tables or the use of micro-windows. Initial retrieval examples on five distinctly different aerosol plumes (fire, sand, volcanic ash, sulphuric acid and ice) demonstrated its ability to reconstruct broadband features observed in the measured spectra.

[50] In order to retrieve aerosol properties accurately (total mass and effective radius), there are two important prerequisites. The first is good knowledge of the size distribution (type and width), while the second is a good knowledge of the refractive index of the measured aerosol. When the assumed refractive index does not exhibit the same spectral features as the observed spectra the optimal estimation iteration is unlikely to converge (or convergence is only possible when taking into account an unrealistically high instrumental noise, as we will demonstrate further on). Other less important factors that affect the accuracy of the retrieval are the assumed aerosol altitude, layer thickness, surface temperature and instrumental noise.

[51] Figure 10 shows (in blue) part of a measured IASI spectrum observed around 11.27 UTC on 17 May above the North Sea ( $54.79^\circ\text{N}$ ,  $0.69^\circ\text{E}$ ). A distinct V-shape absorption

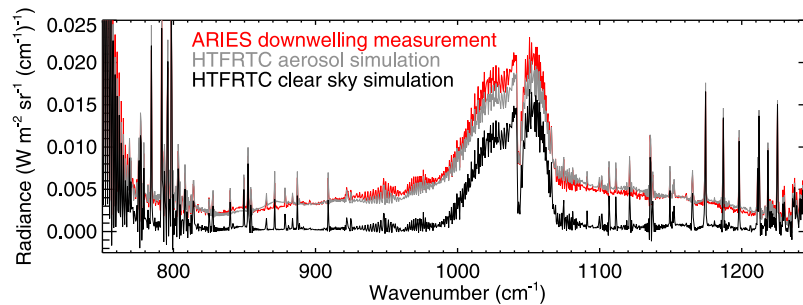


**Figure 9.** Comparison of ARIES downwelling radiance measurement during FAAM flight on 17 May 2010 showing average radiance (red) recorded during two runs under the ash layer at 3150 m altitude. A simulation (gray) has been computed using an average lidar vertical extinction profile, constrained by the radiance measurement to an effective AOD of 0.33. A clear sky simulation (black) indicates the radiance that would be observed in the absence of an ash layer. The FAAM (A) set of optical properties has been used in the HTFRTC simulation.

feature can be distinguished between 800 and 1235  $\text{cm}^{-1}$  which is characteristic of the presence of mineral aerosols [DeSouza-Machado *et al.*, 2006] (not to be confused with the ozone absorption around 1050  $\text{cm}^{-1}$ , here shown in the gray shaded rectangle). A comparison with Figure 5 shows that essentially the same ash spectral signature is seen in both the ARIES and IASI observations.

[52] For the synthetic reconstruction (shown in red) we have used the size distribution as determined from in situ CAS and PCASP measurements (FAAM (A) parameters in Table 1) while the assumed refractive indices were taken from Balkanski *et al.* [2007] corresponding to desert dust with a 1.5% hematite content. The layer height (5 km) and thickness (1.5 km) used in the retrieval were idealized based on the set of lidar extinction profiles retrieved for this date. The surface temperature was taken from the IASI level 2 products as disseminated by EumetCast. The remaining parameters (total aerosol loading, humidity, ozone profiles and  $\text{SO}_2$  total columns) were treated as unknown and constitute the retrieved properties. As can be seen from the

residual (light green) in Figure 10, the fit is good throughout the fitting region, and captures the large scale absorption in the atmospheric window; it does, however, miss out on some of the finer features. This manifests itself also in the RMS of the residual which is about twice IASI's instrumental noise. Also shown in Figure 10 is a reconstruction of how the observed spectrum would have looked (light red) without the aerosol contribution (residual in dark green).

[53] Traditionally, ash retrievals of infrared spectra use one of three sets (andesite, basalt or obsidian) of refractive indices obtained by Pollack *et al.* [1973] from optical measurements on slices of rock samples. The optical properties of rock are arguably very different from airborne particles. Unfortunately, there have been almost no measurements of refractive indices of volcanic ash (as aerosol) and those that were reported were measured at visible and ultraviolet wavelengths [e.g., Patterson *et al.*, 1983]. Until today the refractive index data of Pollack is therefore used in e.g., the retrieval of mass loadings from infrared broadband instruments [Stohl *et al.*, 2011; M. Pavolonis and J. Sieglaff,

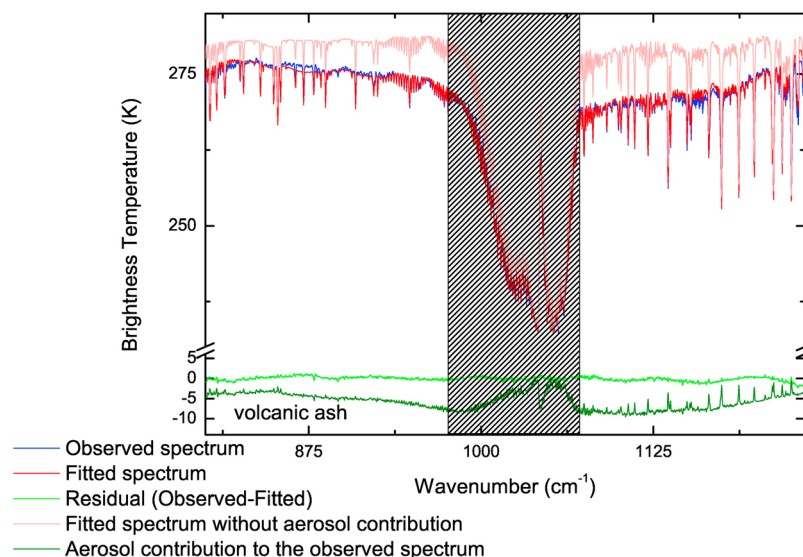


**Figure 10.** Example IASI observation and fit (measured brightness temperature spectra and residuals; see legend).

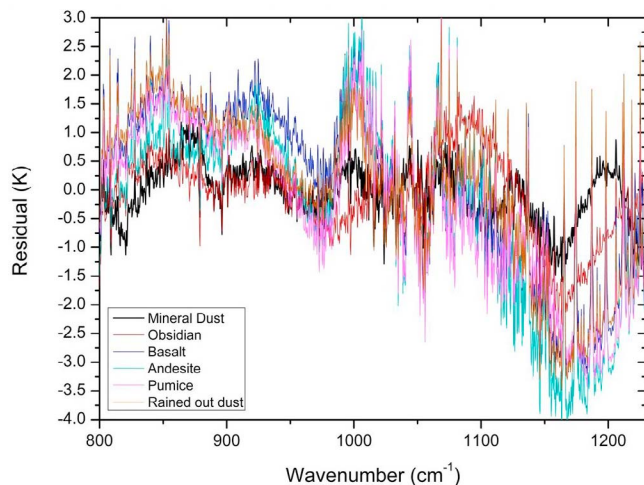


**Figure 11.** Residuals of the same fit as in Figure 10 but with different refractive indices.

GOES-R Advanced Baseline Imager (ABI) Algorithm Theoretical Basis Document For Volcanic Ash (Detection and Height), 2009, available at [http://www.goes-r.gov/products/ATBDs/volcanic\\_ash.pdf](http://www.goes-r.gov/products/ATBDs/volcanic_ash.pdf).

[54] The reason why we have used refractive indices of *Balkanski et al.* [2007] is that the fits obtained with these indices are better than any of the other refractive indices we have tried. This is in spite of the fact that the refractive indices were calculated to represent the refractive index of windblown sand from desert regions (Sahara, Arabian and Gobi). The residuals of six fits with differing refractive indices are shown in Figure 11. For the mineral dust refractive indices of *Balkanski et al.* and the obsidian refractive indices IASI’s instrumental noise was set at  $3 \times 10^{-6} \text{ W m}^{-2} \text{ m sr}^{-1}$ , close to real instrumental noise. For the other indices this led to diverging fits; we therefore needed to use a larger virtual noise of  $1.3 \times 10^{-5} \text{ W m}^{-2} \text{ m sr}^{-1}$  to make the fits converge.

[55] From the residuals, it is clear that the region 1050 to 1250  $\text{cm}^{-1}$  is modeled worst overall for the set of different indices considered here. The mineral dust and obsidian refractive indices result in fits with residuals generally oscillating close to zero; for the other refractive indices there is a marked tendency for positive residuals near 800–900  $\text{cm}^{-1}$  and negative residuals around 1150–1200  $\text{cm}^{-1}$ . Mineral dust and obsidian subsequently yield the smallest RMS of the residual (see Table 2). This is counterintuitive, as measurements of direct samples of Eyjafjallajökull ash indicate a trachyandesitic composition [*Allard et al.*, 2010] and one would therefore expect the andesite refractive index to yield the best fit. Using different refractive indices has a considerable effect on total retrieved masses in Table 2, up to 100% between the lowest and highest values. Future experimental measurements leading to new, independent and public data sets of refractive indices of different types of volcanic ash would therefore be highly desirable.

[56] We note that there are small spectral signatures found in the ash which are unaccounted for in the available refractive indices for this and other eruptions. To emphasize this point, we present two examples in Figure 12 where mass loading and particle radius have been fitted to IASI spectra

observed from recent eruptions (Grímsvötn in Iceland and Puyehue in Chile). These volcanoes produced ash with very different characteristics to the trachyandesite ash produced by Eyjafjallajökull. Grímsvötn produced basaltic ash, while Puyehue produced (at least in the initial phase) rhyodacitic ash. The fits were performed for Grímsvötn and Puyehue with, respectively, refractive indices of basalt and rhyolitic obsidian from *Pollack et al.* [1973]. It is apparent that while the overall spectral shape is captured for both examples, different features remain unaccounted for with the potential for introducing errors in an ash retrieval scheme.

[57] We have also tested the sensitivity of the IASI mass retrievals to different assumptions of PSD. In the same way as for our analysis of SHIMS, BBR and ARIES data in section 3 we consider the three sets of parameters detailed in Table 1. Taking the *Balkanski et al.* [2007] mineral dust case in Table 2 as our default FAAM (A) case we find that a different choice of PSD leads to a relative mass retrieval of 109% (FAAM (B)) and 206% (DLR). Thus, using the DLR PSD in the retrieval produces a markedly higher mass estimate than the FAAM (A) and (B) cases.

[58] We have performed the retrievals as in Figure 10 for all spectra measured on the 17 May 2010 above northern Europe and the North Sea which passed the ash correlation detection test [*Clarisse et al.*, 2010b]. The results are summarized in Figure 13. The largest values were found to be  $2.5 \text{ g/m}^2$  while total masses were 370 and 300 kT respectively for the morning and evening orbit.

[59] It is instructive to compare IASI retrievals of mass loading with those derived from other sources, particularly from the lidar data recorded during the period 14:15 to 16:30 UTC on 17 May 2010. This period occurs mid-way between the IASI morning and evening overpass times. Our data analysis proceeded as follows: an area was selected within which lidar measurements of the ash layer over the North Sea were obtained: the area has dimensions  $3.3^\circ$  longitude by  $1.0^\circ$  latitude and includes the locations labeled as ‘2’ and ‘3’ in Figure 4. SEVIRI RGB dust product imagery at 15 min intervals was then used to monitor the speed of advection of the ash by the prevailing winds. Finally, the data selection area was moved spatially according to the position of the ash on the SEVIRI imagery to coincide with the times of the IASI morning and evening orbits. In this way we can select IASI fields of view (FOVs) which relate approximately to the same area of the ash cloud. We note that this analysis cannot account for temporal variations in the ash distribution that deviate from a simple translation of position.

**Table 2.** Results of Fits to IASI Observations Using Differing Refractive Indices

Name	RMS of Residual (in $\text{W m}^{-2} \text{ m sr}^{-1}$ )	Mass (in % of first)	Reference
Mineral dust	$5.5 \times 10^{-6}$	100	<i>Balkanski et al.</i> [2007]
Obsidian	$7.2 \times 10^{-6}$	79	<i>Pollack et al.</i> [1973]
Basalt	$1.6 \times 10^{-5}$	65	<i>Pollack et al.</i> [1973]
Andesite	$1.5 \times 10^{-5}$	63	<i>Pollack et al.</i> [1973]
Pumice	$1.4 \times 10^{-5}$	73	<i>Volz</i> [1973]
Rained out dust	$1.5 \times 10^{-5}$	159	<i>Volz</i> [1973]

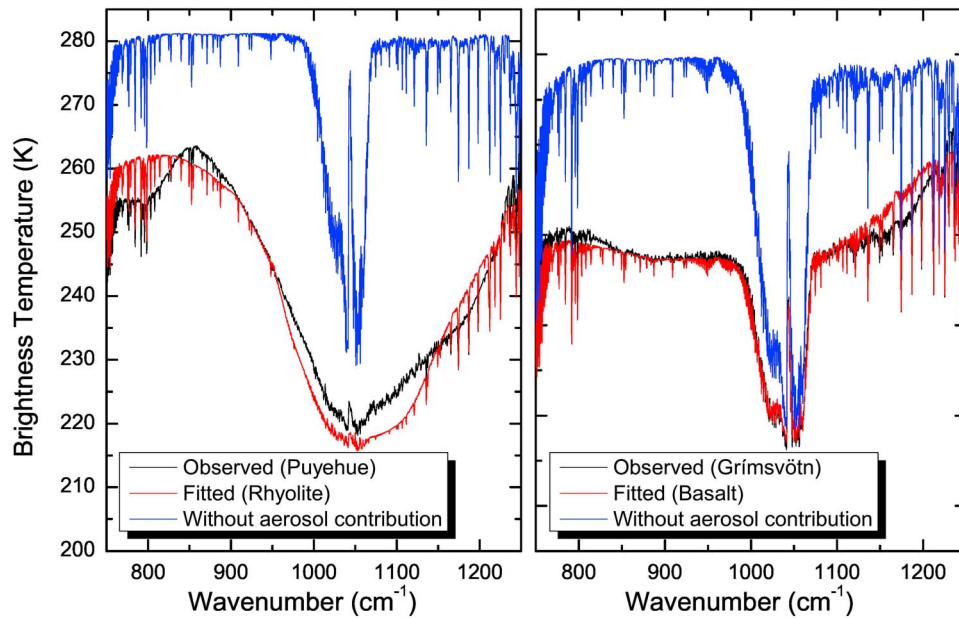


**Figure 12.** Fits to IASI observations of volcanic ash (c.f. Figure 10) for eruptions from (left) Puyehue-Cordón Caulle in Chile in June 2011 and (right) Grímsvötn in Iceland in May 2011. Observed brightness temperatures (black) are compared with fitted (red) and clear-air (blue) simulations. Refractive indices for rhyolite were used for Puyehue whereas data for basalt were used for the Grímsvötn fit.

[60] In Figures 14a and 14b, IASI retrievals of ash mass column loading for morning and evening overpasses respectively are compared with those derived from lidar backscatter returns within the displaced selected area. In these plots the ash particles have been assumed to be spheres in the lidar derivation. Considering the uncertainties involved in both the IASI and lidar mass retrievals the level of agreement between the two sets of histograms is encouraging. For the IASI morning orbit some FOVs give relatively high ( $>1.0 \text{ g/m}^2$ ) mass retrievals which are not replicated in the lidar results. For the evening orbit the histograms show a greater degree of overlap.

[61] The sensitivity of the lidar mass estimates to assumed particle shape is investigated in Figures 14c and 14d, where

the lidar column mass has now been derived assuming the irregular particle model. Treating ash particles as irregular shapes rather than spheres decreases the lidar derived mass by around 30% for this flight [see *Marengo et al.*, 2011]. Qualitatively, in the case of the IASI evening overpass the agreement with the lidar data is enhanced by using the non-spherical model, while for the morning overpass some outliers remain. To test whether the IASI and lidar (spherical and irregular) histograms are significantly different in a statistical sense the Whitney-Mann U test has been applied to the IASI-lidar(sphere) and IASI-lidar(irregular) histograms. This quantitative non-parametric test assesses whether there is a bias to larger values in either the spherical or irregular lidar mass histograms relative to IASI. It is found statistically

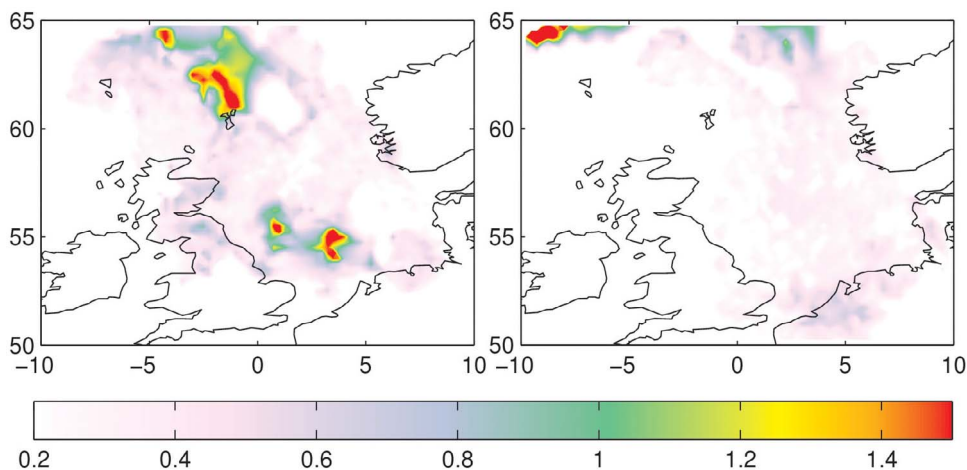


**Figure 13.** IASI ash mass loadings (in  $\text{g/m}^2$ ) on 17 May 2010. (left) The morning orbit includes data around 09:48 and 11:28 UTC, while (right) the evening orbit includes overpasses near 19:37 and 21:17 UTC.

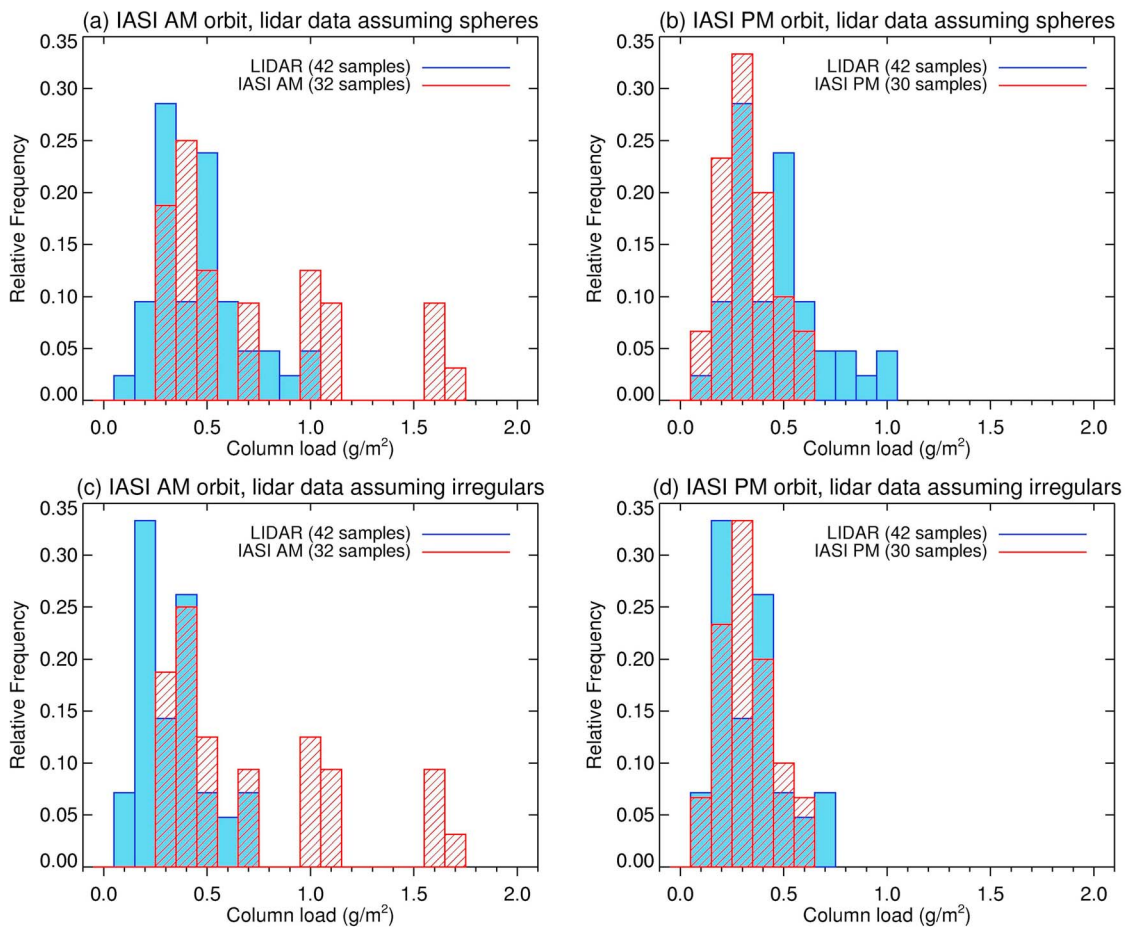


**Figure 14.** Histogram comparison of aerosol mass column loading retrievals from IASI (hatched bins) and FAAM BAe 146 lidar (filled bins). The IASI retrievals are based on the FAAM (A) irregular model PSD. (a) Mass loadings corresponding to IASI morning orbit on 17 May 2011; lidar estimates based on assumption of spherical particles. (b) Mass loadings for IASI evening orbit, lidar estimates based on spheres. (c, d) As in Figures 14a and 14b, but lidar estimates are based on assumption of irregularly shaped particle model.

(at the 95% level of confidence using a two-tailed test) that the spherical and irregular histograms are not significantly different from the IASI histogram for both the morning and evening cases.

[62] Given the uncertainties in tracking the ash cloud in the SEVIRI imagery, and the possibility of temporal variations in the ash density, the agreement of IASI and lidar mass estimates in Figure 14, based on observations separated in time by several hours, is remarkable. Further corroboration of the IASI mass retrievals comes from the in situ data analysis of *Turnbull et al.* [2012] for this case study: for four profiles (ascents and descents) through the ash layer the column ash loading estimated from FAAM CAS measurements (default irregular model) was between 0.22 and 0.71  $\text{g/m}^2$ . Coterminous measurements with the nephelometer probe produced estimates of 0.29–0.72  $\text{g/m}^2$ . These values are entirely consistent with the lidar and IASI histograms presented in Figure 14. Taken together, these results represent a convincing validation of the IASI aerosol retrieval algorithm.

[63] We cannot show conclusively from Figure 14 that the irregular particle model gives superior mass estimates.

Nevertheless, electron-microscope images and scattering patterns from the SID-2H probe did indicate that the ash particles were highly irregular in shape (*Johnson et al.*, submitted manuscript, 2011). For this reason we take the modeling for irregular particles as our best estimate of ash properties for this 17 May 2010 case study.

## 5. Conclusions

[64] The Eyjafjallajökull eruption afforded a valuable opportunity to determine in situ properties of volcanic ash in conjunction with lidar backscatter measurements and observations of longwave and shortwave radiation. We have focused here and in our companion paper [*Turnbull et al.*, 2012] on measurements from 17 May 2010 where the ash cloud was advected over the southern North Sea in otherwise clear sky conditions. This presented an ideal case study, as the presence of water or ice cloud would have complicated our analysis considerably. We believe the unique combination of instrumentation on the FAAM BAe 146 atmospheric research aircraft makes this a valuable data set with which to test our understanding of volcanic ash microphysical and

radiative properties. Indeed, our experience of flying with this configuration during April–May 2010 was vital in influencing the choice of instrumentation for the dedicated Met Office Civil Contingency Aircraft (MOCCA) first flown in 2011.

[65] Our testing of rival models of lognormal PSDs reveals that modeled solar and terrestrial optical properties are not particularly sensitive to assumptions of irregular or spherical particles used when deriving the size distribution. Thus, we can reproduce ARIES spectral radiances in the longwave and SHIMS spectral irradiances in the shortwave with either assumption, using Mie-Lorenz calculations of optical properties. However, results depend strongly on the aircraft data set used to define the PSD. Radiative closure was less successful using the aerosol size distribution derived from ash measurements made by the DLR Falcon aircraft FSSP instrument. As a result of the more absorbing refractive index assumed in the analysis of the DLR FSSP data, the PSD from the DLR aircraft is broader, and peaks at a higher mean diameter, producing longwave effects that were much stronger relative to the shortwave making the modeled aerosol optical properties incompatible with the combination of remote sensing measurements presented in this study. For example, when applied to IASI mass retrievals, mass estimates are approximately doubled when using the FSSP PSD in preference to the CAS PSD. As noted above, there are many uncertainties in accurately representing refractive indices across both the solar and terrestrial spectrum owing to the complex mixing state of coarse and fine mode particles which impact particle scattering and absorption and hence the size distribution determined from the optical particle counters. Further case studies combining the in situ and radiative transfer measurements such as this one are certainly required before general conclusions about the ability of optical particle counters to accurately represent PSDs and radiative properties of volcanic ash can be drawn.

[66] Estimates of aerosol mass column loadings from shortwave measurements exhibit a sensitivity to particle shape. This is due to dependencies of the specific extinction coefficient  $k_{\text{ext}}$  (which relates the mass of aerosol to the optical extinction) and the coarse extinction fraction  $f_c$  on the interpretation of optical particle counter measurements (Johnson et al., submitted manuscript, 2011). For the lidar and CAS column mass estimates the assumption of spheres rather than irregular particles increases the derived mass by approximately 30%. By contrast, Yang et al. [2007] report very small sensitivity of retrieved aerosol parameters on particle non-sphericity at thermal infrared wavelengths. Our results here with ARIES and IASI observations confirm this overall finding, with very small sensitivity of the 8–13  $\mu\text{m}$  infrared spectrum on particle shape. Comparing the IASI retrievals with assumptions of spherical or irregular coarse mode particles results in only a minor (9%) change in derived column mass.

[67] The sensitivity of infrared ARIES spectra to the presence of volcanic ash has been demonstrated, with a clear relationship between lidar AOD and brightness temperature signatures. A very simple spectral gradient diagnostic is shown to be well correlated with collocated AODs. The lidar extinction is proportional to the mass density of the ash [Marenco et al., 2011]; thus, we have established empirically the direct link between aerosol mass and infrared

brightness temperatures. Our results for a sophisticated retrieval algorithm for IASI show that it is possible to derive ash mass loadings in good agreement with those determined from the airborne lidar. The IASI mass estimates are also consistent with values derived from intercepts of the ash cloud with the FAAM BAe 146 using optical particle counter and nephelometer scattering measurements. To our knowledge this is the first independent verification of a hyperspectral aerosol retrieval scheme, and gives confidence in the ability to retrieve key parameters such as aerosol mass from infrared space-borne sounders.

[68] The use of mineral dust refractive indices due to Balkanski et al. [2007] and CAS in situ measured PSD is shown to be successful in reproducing the spectral signature of ash from this eruption across the infrared (8–13  $\mu\text{m}$ ) to visible/UV (0.3–1.7  $\mu\text{m}$ ) spectral range. We have achieved, therefore, a reasonable degree of radiative closure between radiation measurements, in situ data used to derive optical properties of the ash, and lidar observations of the vertical extinction and radiative transfer simulations. While the use of Balkanski et al. [2007] refractive indices has led to the optimal agreement in this specific case, we acknowledge that the refractive indices of the volcanic plume from Eyjafjallajökull may change significantly during the course of the eruption as evidenced by the airborne measurements made by Schumann et al. [2011] and the retrievals of volcanic ash from satellites [Millington et al., 2012]. This complexity in terms of refractive index is an obvious barrier to satellite retrievals, but the use of high spectral resolution instrumentation such as the aircraft-borne ARIES and satellite-borne IASI sensors in minimizing modeled and measured spectral differences shows some promise. With reference also to Figure 12 we caution that the optical properties are shown to be acutely sensitive to the characteristic ash composition for each eruption, particularly in terms of the aerosol refractive index and PSD. This motivates the need for a better understanding of the variability of volcanic ash mineralogy and improved measurements of refractive indices.

[69] **Acknowledgments.** Airborne data were obtained using the BAe 146-301 Atmospheric Research Aircraft (ARA) flown by Directflight Ltd. and managed by the Facility for Airborne Atmospheric Measurements (FAAM), which is a joint entity of the Natural Environment Research Council (NERC) and the Met Office. The CAPS instrument was provided through the Facility for Ground-based Atmospheric Measurement (FGAM) by Martin Gallagher, Hugh Coe and James Dorsey at the Centre for Atmospheric Science, University of Manchester. IASI has been developed and built under the responsibility of the Centre National d'Etudes Spatiales (CNES, France). It is flown onboard the Metop satellites as part of the EUMETSAT Polar System. The IASI L1 data are received through the EUMETCast near real time data distribution service. L. Clarisse is Postdoctoral Researcher with F.R.S.-FNRS.

## References

- Allard, P., M. R. Burton, N. Oskarsson, A. Michel, and M. Polacci (2010), Chemistry and fluxes of magmatic gases powering the explosive trachyandesitic phase of Eyjafjallajökull 2010 eruption: Constraints on degassing magma volumes and processes, Abstract V53F-07 presented at 2010 Fall Meeting, AGU, San Francisco, Calif., 13–17 Dec.
- Ansmann, A., et al. (2010), The 16 April 2010 major volcanic ash plume over central Europe: EARLINET lidar and AERONET photometer observations at Leipzig and Munich Germany, *Geophys. Res. Lett.*, *37*, L13810, doi:10.1029/2010GL043809.
- Balkanski, Y., M. Schulz, T. Claquin, and S. Guibert (2007), Reevaluation of Mineral aerosol radiative forcings suggests a better agreement with satellite and AERONET data, *Atmos. Chem. Phys.*, *7*, 81–95, doi:10.5194/acp-7-81-2007.

- Benassi, M., R. D. M. Garcia, A. H. Karp, and C. E. Siewert (1984), A high-order spherical harmonics solution to the standard problem in radiative transfer, *Astron. J.*, *280*, 853–864.
- Brindley, H. E., and A. Ignatov (2006), Retrieval of mineral aerosol optical depth and size information from Meteosat Second Generation SEVIRI solar reflectance bands, *Remote Sens. Environ.*, *102*, 344–363, doi:10.1016/j.rse.2006.02.024.
- Clarisse, L., P. F. Coheur, A. J. Prata, D. Hurtmans, A. Razavi, T. Phulpin, J. Hadji-Lazaro, and C. Clerbaux (2008), Tracking and quantifying volcanic SO<sub>2</sub> with IASI, the September 2007 eruption at Jebel at Tair, *Atmos. Chem. Phys.*, *8*(24), 7723–7734, doi:10.5194/acp-8-7723-2008.
- Clarisse, L., D. Hurtmans, A. J. Prata, F. Karagulian, C. Clerbaux, M. D. Mazière, and P.-F. Coheur (2010a), Retrieving radius, concentration, optical depth, and mass of different types of aerosols from high-resolution infrared nadir spectra, *Appl. Opt.*, *49*, 3713–3722, doi:10.1364/AO.49.003713.
- Clarisse, L., F. Prata, J.-L. Lacour, D. Hurtmans, C. Clerbaux, and P.-F. Coheur (2010b), A correlation method for volcanic ash detection using hyperspectral infrared measurements, *Geophys. Res. Lett.*, *37*, L19806, doi:10.1029/2010GL044828.
- Clerbaux, C., et al. (2009), Monitoring of atmospheric composition using the thermal infrared IASI/MetOp sounder, *Atmos. Chem. Phys.*, *9*, 6041–6054, doi:10.5194/acp-9-6041-2009.
- Clough, S. A., M. W. Shephard, E. Mlawer, J. S. Delamere, M. Iacono, K. Cady-Pereira, S. Boukabara, and P. D. Brown (2005), Atmospheric radiative transfer modeling: A summary of the AER codes, *J. Quant. Spectrosc. Radiat. Transf.*, *91*(2), 233–244, doi:10.1016/j.jqsrt.2004.05.058.
- Cox, C., and W. Munk (1954), Measurement of the roughness of the sea surface from photographs of the Sun's glitter, *J. Opt. Soc. Am.*, *44*, 838–850, doi:10.1364/JOSA.44.000838.
- Dacre, H. F., et al. (2011), Evaluating the structure and magnitude of the ash plume during the initial phase of the 2010 Eyjafjallajökull eruption using lidar observations and NAME simulations, *J. Geophys. Res.*, *116*, D00U03, doi:10.1029/2011JD015608.
- DeSouza-Machado, S., L. Strow, S. Hannon, and H. Motteler (2006), Infrared dust spectral signatures from AIRS, *Geophys. Res. Lett.*, *33*, L03801, doi:10.1029/2005GL024364.
- Edwards, J. M., and A. Slingo (1996), Studies with a flexible new radiation code. I: Choosing a configuration for a large-scale model, *Q. J. R. Meteorol. Soc.*, *122*(531), 689–719, doi:10.1002/qj.49712253107.
- Francis, P. N., M. C. Cooke, and R. W. Saunders (2012), Retrieval of physical properties of volcanic ash using Meteosat: A case study from the 2010 Eyjafjallajökull eruption, *J. Geophys. Res.*, *117*, D00U09, doi:10.1029/2011JD016788.
- Gangale, G., A. J. Prata, and L. Clarisse (2010), The infrared spectral signature of volcanic ash determined from high-spectral resolution satellite measurements, *Remote Sens. Environ.*, *114*(2), 414–425, doi:10.1016/j.rse.2009.09.007.
- Guffanti, M., T. J. Casadevall, and K. Budding (2010), Encounters of aircraft with volcanic ash clouds: A compilation of known incidents, 1953–2009, *U.S. Geol. Surv. Data Ser. 545*, version 1.0, 12 pp., U.S. Geol. Surv., Reston, Va.
- Havemann, S. (2006), The development of a fast radiative transfer model based on an Empirical Orthogonal Functions (EOF) technique, *Proc. SPIE Int. Soc. Opt. Eng.*, *6405*, 64050, doi:10.1117/12.693995.
- Havemann, S., and A. J. Baran (2001), Extension of T-matrix to scattering of electromagnetic plane waves by non-axisymmetric dielectric particles: Application to hexagonal cylinders, *J. Quant. Spectrosc. Radiat. Transf.*, *70*, 139–158, doi:10.1016/S0022-4073(00)00127-8.
- Havemann, S., J. C. Thelen, J. P. Taylor, and A. Keil (2009), The Havemann-Taylor Fast Radiative Transfer Code: Exact fast radiative transfer for scattering atmospheres using Principal Components (PCs), *AIP Conf. Proc.*, *1100*, 38–40, doi:10.1063/1.3117000.
- Haywood, J. M., P. N. Francis, M. D. Glew, and J. P. Taylor (2001), Optical properties and direct radiative effect of Saharan dust: A case study of two Saharan dust outbreaks using aircraft data, *J. Geophys. Res.*, *106*(D16), 18,417–18,430, doi:10.1029/2000JD900319.
- Haywood, J. M., P. N. Francis, S. R. Osborne, M. D. Glew, N. Loeb, E. J. Highwood, D. Tanré, G. Myhre, P. Formenti, and E. Hirst (2003), Radiative properties and direct radiative effect of Saharan dust measured by the C-130 aircraft during SHADE: 1. Solar spectrum, *J. Geophys. Res.*, *108*(D18), 8577, doi:10.1029/2002JD002687.
- Haywood, J. M., et al. (2010), Observations of the eruption of the Sarychev Volcano and simulations using the HadGEM2 climate model, *J. Geophys. Res.*, *115*, D21212, doi:10.1029/2010JD014447.
- Haywood, J., B. Johnson, S. Osborne, J. Mulcahy, M. Brooks, M. Harrison, S. Milton, and H. Brindley (2011), Observations and modelling of the solar and terrestrial radiative effects of Saharan dust: A radiative closure case-study over oceans during the GERBILS campaign, *Q. J. R. Meteorol. Soc.*, *137*(658), 1211–1226, doi:10.1002/qj.770.
- Hsu, N. C., S. C. Tsay, M. D. King, and J. R. Herman (2006), Deep blue retrievals of Asian aerosol properties during ACE-Asia, *IEEE Trans. Geosci. Remote Sens.*, *44*, 3180–3195, doi:10.1109/TGRS.2006.879540.
- Intergovernmental Panel on Climate Change (2007), *Climate Change 2007: The Physical Science Basis. Contribution of Working Group I to the Fourth Assessment Report of the Intergovernmental Panel on Climate Change*, edited by S. Solomon et al., Cambridge Univ. Press, Cambridge, U. K.
- Kahn, R., P. Banerjee, and D. McDonald (2001), Sensitivity of multiangle imaging to natural mixtures of aerosols over ocean, *J. Geophys. Res.*, *106*(D16), 18,219–18,238, doi:10.1029/2000JD900497.
- Liu, X., W. L. Smith, D. K. Zhou, and A. Larar (2006), Principal component-based radiative transfer model for hyperspectral sensors: Theoretical concept, *Appl. Opt.*, *45*(1), 201–209, doi:10.1364/AO.45.000201.
- Loeb, N. G., and S. Kato (2002), Top-of-atmosphere direct radiative effect of aerosols over the tropical oceans from the Clouds and the Earth's Radiant Energy System (CERES) satellite instrument, *J. Clim.*, *15*, 1474–1484, doi:10.1175/1520-0442(2002)015<1474:TOADRE>2.0.CO;2.
- Marengo, F., B. Johnson, K. Turnbull, S. Newman, J. Haywood, H. Webster, and H. Ricketts (2011), Airborne lidar observations of the 2010 Eyjafjallajökull volcanic ash plume, *Journal of Geophysical Research, J. Geophys. Res.*, *116*, D00U05, doi:10.1029/2011JD016396.
- McClatchey, R. A., R. W. Fenn, J. E. A. Selby, F. E. Volz, and J. S. Garing (1972), *Optical Properties of the Atmosphere*, 3rd ed., AFCRL-72-0497, 113 pp., Air Force Cambridge Res. Lab., L. G. Hanscom Field, Bedford, Mass.
- Millington, S. C., R. Saunders, P. Francis, and H. N. Webster (2012), Simulated volcanic ash imagery: A method to compare NAME ash concentration forecasts with SEVIRI imagery for the Eyjafjallajökull eruption in 2010, *J. Geophys. Res.*, doi:10.1029/2011JD016770, in press.
- Mishchenko, M. I., et al. (1999), Aerosol retrievals over the ocean by use of channels 1 and 2 AVHRR data: Sensitivity analysis and preliminary results, *Appl. Opt.*, *38*, 7325–7341, doi:10.1364/AO.38.007325.
- Newman, S. M., J. A. Smith, M. D. Glew, S. M. Rogers, and J. P. Taylor (2005), Temperature and salinity dependence of sea surface emissivity in the thermal infrared, *Q. J. R. Meteorol. Soc.*, *131*(610), 2539–2557, doi:10.1256/qj.04.150.
- Osborne, S. R., A. J. Baran, B. T. Johnson, J. M. Haywood, E. Hesse, and S. Newman (2011), Short-wave and long-wave radiative properties of Saharan dust aerosol, *Q. J. R. Meteorol. Soc.*, *137*(658), 1149–1167, doi:10.1002/qj.771.
- Patterson, E. M., C. O. Pollard, and I. Galindo (1983), Optical properties of the ash from El Chichón Volcano, *Geophys. Res. Lett.*, *10*(4), 317–320, doi:10.1029/GL010i004p00317.
- Pollack, J., O. Toon, and B. Khare (1973), Optical properties of some terrestrial rocks and glasses, *Icarus*, *19*, 372–389, doi:10.1016/0019-1035(73)90115-2.
- Prata, A. J., and I. F. Grant (2001), Retrieval of microphysical and morphological properties of volcanic ash plumes from satellite data: Application to Mt Ruapehu, New Zealand, *Q. J. R. Meteorol. Soc.*, *127*(576), 2153–2179, doi:10.1002/qj.49712757615.
- Prata, A. J., and J. Kerkmann (2007), Simultaneous retrieval of volcanic ash and SO<sub>2</sub> using MSG-SEVIRI measurements, *Geophys. Res. Lett.*, *34*, L05813, doi:10.1029/2006GL028691.
- Prata, A. J., G. Gangale, L. Clarisse, and F. Karagulian (2010), Ash and sulfur dioxide in the 2008 eruptions of Okmok and Kasatochi: Insights from high spectral resolution satellite measurements, *J. Geophys. Res.*, *115*, D00L18, doi:10.1029/2009JD013556.
- Remer, L. A., and Y. J. Kaufman (2006), Aerosol direct radiative effect at the top of the atmosphere over cloud free oceans derived from four years of MODIS data, *Atmos. Chem. Phys.*, *6*, 237–253, doi:10.5194/acp-6-237-2006.
- Ringer, M. A., J. M. Edwards, and A. Slingo (2003), Simulation of satellite channel radiances in the Met Office Unified Model, *Q. J. R. Meteorol. Soc.*, *129*(589), 1169–1190, doi:10.1256/qj.02.61.
- Schumann, U., et al. (2011), Airborne observations of the Eyjafjalla Volcano ash cloud over Europe during air space closure in April and May 2010, *Atmos. Chem. Phys.*, *11*, 2245–2279, doi:10.5194/acp-11-2245-2011.
- Stohl, A., et al. (2011), Determination of time- and height-resolved volcanic ash emissions for quantitative ash dispersion modeling: The 2010 Eyjafjallajökull eruption, *Atmos. Chem. Phys. Discuss.*, *11*, 5541–5588, doi:10.5194/acpd-11-5541-2011.
- Turnbull, K. F., B. T. Johnson, F. Marengo, J. M. Haywood, A. Minikin, B. Weinzierl, H. Schlager, U. Schumann, S. J. Leadbetter, and A. M. Woolley (2012), A case study of observations of volcanic ash from the

- Eyjafjallajökull eruption: 1. In situ airborne observations, *J. Geophys. Res.*, doi:10.1029/2011JD016688, in press.
- Volz, F. (1973), Infrared optical constants of ammonium sulfate, Sahara dust; volcanic pumice and flyash, *Appl. Opt.*, 12, 564–568, doi:10.1364/AO.12.000564.
- Watkin, S. C. (2003), The application of AVHRR data for the detection of volcanic ash in a Volcanic Ash Advisory Centre, *Meteorol. Appl.*, 10(4), 301–311, doi:10.1017/S1350482703001063.
- Wilson, S. H. S., N. C. Atkinson, and J. A. Smith (1999), The development of an airborne infrared interferometer for meteorological sounding studies, *J. Atmos. Oceanic Technol.*, 16(12), 1912–1927, doi:10.1175/1520-0426(1999)016<1912:TDOAAI>2.0.CO;2.
- Witham, C. S., M. C. Hort, R. Potts, R. Servranckx, P. Husson, and F. Bonnardot (2007), Comparison of VAAC atmospheric dispersion models using the 1 November 2004 Grimsvötn eruption, *Meteorol. Appl.*, 14, 27–38, doi:10.1002/met.3.
- Yang, P., Q. Feng, G. Hong, G. W. Kattawar, W. J. Wiscombe, M. I. Mishchenko, O. Dubovik, I. Laszlo, and I. N. Sokolik (2007), Modeling of the scattering and radiative properties of nonspherical dust-like aerosols, *J. Aerosol Sci.*, 38, 995–1014, doi:10.1016/j.jaerosci.2007.07.001.
- 
- A. J. Baran, S. Havemann, B. Johnson, F. Marengo, S. M. Newman, D. O’Sullivan, and K. Turnbull, Observation Based Research, Met Office, FitzRoy Road, Exeter EX1 3PB, UK. (stu.newman@metoffice.gov.uk)
- L. Clarisse and D. Hurtmans, Spectroscopie de l’Atmosphère, Service de Chimie Quantique et Photoscopique, ULB, 50 ave. F. D. Roosevelt, B-1050 Brussels, Belgium.
- J. Haywood, College of Engineering, Mathematics, and Physical Science, University of Exeter, Exeter EX4 4QF, UK.